6,1



RESEARCH MEMORANDUM

A SUMMARY OF THE LONGITUDINAL AND LATERAL STABILITY AND CONTROL CHARACTERISTICS OBTAINED FROM ROCKET-MODEL

TESTS OF A SWEPT-WING FIGHTER-TYPE AIRPLANE

AT MACH NUMBERS FROM 0.5 TO 1.9

By Grady L. Mitcham√

Langley Aeronautical Laboratory Langley Field, Va.

LIBRARY COPY

MAR 14 1957

LANGLEY AERONAUTICAL LABORATORY
LIBRARY, NACA
LANGLEY FILL D. VIRGINIA

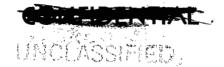
CLASSIFIED DOCUMENT

This material contains information affecting the National Defense of the United States within the meaning of the espionage laws, Title 18, U.S.C., Secs. 793 and 794, the transmission or revelation of which in any manner to an unauthorized person is prohibited by law.

NATIONAL ADVISORY COMMITTEE FOR AERONAUTICS

WASHINGTON

February 27, 1957



NACA RM L56K19



NATIONAL ADVISORY COMMITTEE FOR AERONAUTICS

RESEARCH MEMORANDUM

A SUMMARY OF THE LONGITUDINAL AND LATERAL STABILITY AND CONTROL CHARACTERISTICS OBTAINED FROM ROCKET-MODEL

TESTS OF A SWEPT-WING FIGHTER-TYPE AIRPLANE

AT MACH NUMBERS FROM 0.5 TO 1.9

By Grady L. Mitcham

SUMMARY

A flight investigation has been conducted by means of rocket models of a swept-wing fighter-type airplane to determine drag coefficients, longitudinal and lateral stability derivatives, effects of aeroelasticity on rolling effectiveness, and the effect of the engine jet exhaust on the trim characteristics over the Mach number range from 0.5 to 1.9.

The jet-engine simulator caused a decrease in trim angle of attack of approximately 1.27° and a decrease in trim-lift coefficient of 0.07. A positive increment in pressure coefficient was caused by the jet on the side and bottom of the fuselage. As the distance downstream of the jet exit increased, the increment on the bottom of the fuselage increased, whereas the increments on the side decreased to a negative peak.

The drag rise begins at a Mach number of 0.90. The minimum-drag coefficient (including base and internal drag) has a value of 0.02 at a Mach number of 0.87, an increase to 0.070 at a Mach number of 1.1 and then a gradual increase to a value of 0.074 at a Mach number of 1.83.

There was a reduction in static longitudinal stability at the higher lift coefficients at subsonic speeds. Dynamic longitudinal stability was indicated throughout the speed range.

The horizontal tail was an effective control throughout the speed range. The dihedral effect was adequate. The roll damping was nearly constant through the speed range and agreed with some theoretical values. The aeroelastic losses in rolling effectiveness varied from about 6 percent at 35,000 feet to about 27 percent at sea level at a Mach number of 0.5 and from about 20 percent at 35,000 feet to about 84 percent at sea level at a Mach number of 1.2.

2/15/A CEN #43



INTRODUCTION

As a result of the current interest in airplanes that fly at supersonic speeds, the Pilotless Aircraft Research Division of the Langley Aeronautical Laboratory has conducted an investigation to determine some of the aerodynamic characteristics of a twin-engine, swept-wing, fighter-type airplane by utilization of the rocket-propelled-model technique.

The primary purposes of this investigation were to determine drag coefficients, longitudinal and lateral stability derivatives, effects of aeroelasticity on the rolling effectiveness, and the effect of the engine jet exhaust on the trim characteristics, since the engine exits are located below and well forward of the all-movable horizontal stabilizer and tail.

This paper summarizes the flight-test results obtained from the six models used to determine the desired aerodynamic information over the Mach number range from 0.5 to 1.9.

SYMBOLS

A	cross-sectional area, sq ft
A_e	jet exit area, sq in.
а	total damping factor
a _l /g	longitudinal-accelerometer reading
a _n /g	normal-accelerometer reading
a _t /g	transverse-accelerometer reading
ъ	wing span, ft
ē	mean aerodynamic chord, ft
C _c	chord-force coefficient, positive in a rearward direction, $\frac{a_1}{g} \; \frac{W}{S_W} \; \frac{1}{q}$
c_{D}	drag coefficient, $C_{ m N}$ sin α + $C_{ m C}$ cos α

 $^{\text{C}}_{\text{D,b}}$ base-drag coefficient, $\frac{-(p_{\text{b}}-p_{\text{o}})}{qS_{\text{w}}}$ base area

C_{D,i} internal-drag coefficient

 $C_{\mathrm{D,min}}$ minimum-drag coefficient

 c_h hinge-moment coefficient, $\frac{\text{Hinge moment}}{qS_t\bar{c}_t}$

 C_{T_c} lift coefficient, $C_{
m N}$ cos α - $C_{
m c}$ sin α

 $\left(^{C}L\right) _{C}C_{D}$, min lift coefficient for minimum drag coefficient

 C_{m} pitching-moment coefficient about center of gravity

C_m pitching-moment coefficient about center of gravity at zero angle of attack and horizontal-tail deflection

 $C_{m_{\overline{Q}}} = \partial C_{m} / \partial \left(\frac{\dot{\theta} \overline{c}}{2V} \right)$, per radian

 $C_{m_{\dot{\alpha}}} = \partial C_{m} / \partial \left(\frac{\dot{\alpha} \bar{c}}{2V} \right)$, per radian

 C_{m_q} + $C_{m_{\overset{\bullet}{\alpha}}}$ pitch-damping derivative

 C_N normal-force coefficient, positive toward top of model from model center line, $\frac{\mathbf{a}_n}{g} \, \frac{W}{S_W} \, \frac{1}{q}$

 ΔC_{p} incremental change in pressure coefficient due to power-on, $c_{\mathrm{p,power-on}} - c_{\mathrm{p,power-off}}$

 C_p pressure coefficient, $\frac{(p_1 - p_0)}{q}$

 $\frac{\text{Cl}_{p}}{\frac{\partial C_{l}}{\partial \left(\frac{\text{pb}}{2\text{V}}\right)}}, \text{ per radian}$

coefficient of rolling moment due to yawing velocity, $\frac{\partial C_l}{\partial \left(\frac{rb}{2V}\right)}, \text{ per radian}$

 $c_{l_{\beta}}$ coefficient of rolling moment due to sideslip, $\frac{\partial c_{l}}{\partial \beta}$, per radian

coefficient of yawing moment due to rolling velocity, $\frac{\partial c_n}{\partial \left(\frac{pb}{2V}\right)}, \text{ per radian}$

 c_{n_r} coefficient of yawing moment due to yawing velocity, $\frac{\partial c_n}{\partial \left(\frac{rb}{2V}\right)}$, per radian

 $C_{n_{\beta}}$ coefficient of yawing moment due to sideslip, $\frac{\partial C_{n}}{\partial \beta}$, per radian

 $\frac{c_{n_{\dot{\beta}}}}{\frac{\partial c_{n}}{\partial \left(\frac{\dot{\beta}b}{2V}\right)}}$ coefficient of yawing moment due to sideslipping velocity,

Cy side-force coefficient

 $c_{Y_{\beta}}$ coefficient of side force due to sideslip, $\frac{\partial c_{Y}}{\partial \beta}$, per radian

F thrust, lb

g acceleration due to gravity, 32.2 ft/sec²

 I_X moment of inertia about body roll axis, slug-ft²

Iy moment of inertia about body pitch axis, slug-ft2

 $I_{\rm Z}$ moment of inertia about body yaw axis, slug-ft²

IXZ product of inertia, slug-ft²

l length, ft

M Mach number

M_e	exit Mach number
m	mass of model, slugs
m'	static test couple applied at 0.945b/2 in a plane parallel to the model center line and perpendicular to the wing chord plane, in-lb
P	period of short-period oscillation, sec; or test load applied at station 26.38 measured along the 48.07-percent chord line in figure 44, 1b
р	rolling angular velocity, radian/sec
P _O	free-stream static pressure, lb/sq ft
p _e	jet exit static pressure, lb/sq ft
p ₁	local static pressure, lb/sq ft
P _b	average base static pressure, lb/sq ft
2 <u>V</u>	wing-tip helix angle, radians
P	dynamic pressure, lb/sq ft
R	Reynolds number
r .	yawing angular velocity, radians/sec; or in figure 6 radius of equivalent body of revolution, ft
S	wing area including intercept, sq ft
Т	free-stream static temperature, ^O R
t	time, sec
^t 1/2	time to damp to one-half amplitude, sec

V velocity, ft/sec

V_e equivalent lateral velocity, ft/sec

W weight of model, lb

w mass flow through duct, slugs/sec

wo mass of air flowing through a stream tube of area equal to the inlet-cowl area under free-stream conditions, slugs/sec

x station (measured from nose), ft

angle of attack of fuselage reference line (at model center of gravity), deg

$$\dot{a} = \frac{1}{57.3} \frac{da}{dt}$$

 β angle of sideslip, deg

γ flight-path angle, measured with respect to a horizontal plane, radians

 $\gamma_{\rm e}$ specific heat ratio at jet exit

horizontal-tail deflection, positive trailing edge down, deg; or in figure 44 deflection of 48.07-percent chord line of wing resulting from applied load P, in.

 $\delta_{\rm a}$ deflection of each aileron measured in a plane perpendicular to the aileron hinge line, deg

 δ/P flexural-stiffness parameter in./lb

 ϵ inclination of principal axis, deg

θ' wing angle of twist in a plane parallel to the model center line and perpendicular to the wing chord plane, radians

θ angle between fuselage center line and horizontal, radians

 θ'/m' torsional-stiffness parameter, radians/in-lb

ρ air density, slugs/cu ft

 ϕ roll angle, radians

 ϕ ' fraction of rigid-wing rolling effectiveness retained by the flexible wing

 $1 - \emptyset'$ fractional loss in rolling effectiveness

ψ angle of yaw, radians

ω frequency of the Dutch roll oscillation, radians/sec

 Ω_{CY} phase angle of side-force coefficient to angle of sideslip, radians unless otherwise noted

phase angle of roll rate to angle of sideslip, radians unless otherwise noted

Subscripts:

w wing

t tail

Derivatives are expressed in this manner: $C_{L_{\alpha}} = \frac{\partial C_{L}}{\partial \alpha}$; $C_{h_{\delta}} = \frac{\partial C_{h}}{\partial \delta}$; and so forth.

A dot over a symbol indicates the first derivative with respect to time, and two dots indicate the second derivative with respect to time.

The symbol | | represents the absolute magnitude of the amplitude of a quantity and is always taken to be positive.

All the measured quantities and aerodynamic derivatives are referred to the system of body axes which assumes the X-axis corresponds to the fuselage reference line. (See fig. 1.)

DESCRIPTION OF MODELS

Model A

The fuselage of model A was constructed of steel bulkheads with plastic hatches and wooden fairings forming the contoured body lines. Both the wing and the horizontal tail had swept plan forms. The wing thickness varied from 6.67 percent chord at the root to 5.71 percent chord at the tip. The airfoil sections were NACA 65A007 and NACA 65A006 airfoils modified by extending the chord 5 percent forward of the

16.04-percent-chord line and adding 1.67 percent positive camber. There was 1° of positive incidence between the wing and the model center line. The horizontal stabilizer was fixed at a deflection of -1.2°. Duralumin plates and mahogany fillers made up the wing panels, and stall plates were located at about 70 percent of each semispan. Two pulse rockets were installed forward of the canopy to disturb the model in pitch. The model was essentially the same as that shown in figure 1 with the exception of the wing root inlets which were faired over on model A to facilitate installation of the rocket-motor simulator in the engine ducts which was used to simulate the jet exhaust characteristics of the turbojet engines. These faired inlets can be seen in the photographs shown as figure 2.

Simulation of jet exhaust was accomplished by use of two solid-propellant rocket motors designed according to the method of reference 1. The simulator shown in figure 3 was installed inside the engine ducts. The ducts terminated external to and under the fuselage. The final angle on the curved boattails of the engine ducts was about 25°. The simulator installation was designed to simulate the Pratt & Whitney J57 engine exhaust characteristics at maximum rated power (sonic exit, afterburner on) at a Mach number of 1.5 and an altitude of 35,000 feet. The simulator flight-test performance data corrected to an altitude of 35,000 feet and full scale by the method of reference 1 are presented in table I with the J57 design values for comparison.

A sketch showing the orifice locations where the flight pressure measurements were taken is presented as figure 4.

Model B

The overall construction of model B was essentially the same as that of model A with the exception of the pulsed horizontal stabilizer and the internal ducting. A three-view drawing is shown in figure 1 and a photograph as figure 5. The area distribution and equivalent body of revolution are shown in figure 6. This information is included for pressure-drag correlation at a Mach number of 1.0.

The horizontal stabilizer was solid duralumin and operated in abrupt movements between angles of approximately -2° and -7° . Operation was achieved by a hydraulically actuated piston. A motor-driven cam operating an electric solenoid was used to control the flow of the hydraulic fluid to the piston and to insure proper timing of the pulsing operation.

Hinge moments were measured by means of a deflection beam attached between the push rod of the control system and the torque rod which actuated the horizontal stabilizer. Deflection in the beam was proportional to the moment in the torque rod which changed the inductance in the instrument.

The wing root inlet was unswept and incorporated a boundary-layer bleed. Internal ducting consisted of two separate ducts running through the model with a minimum cross section near each duct exit. A total-pressure rake was mounted slightly forward of this minimum section to obtain data to be used in the calculation of internal drag at supersonic Mach numbers. A fairing was installed in each duct in order to duplicate the location and cross-sectional area of the engines and accessory housings. The internal ducting did not duplicate that of the full-scale airplane; however, the exit-to-entrance area ratio was such as to regulate the mass flow to approximate the engine requirements at supersonic speeds. Since the afterburner base of the model did not duplicate that of the full-scale airplane, it was necessary to determine the base drag of the model. Six manifold static-pressure tubes were used to determine the average static-pressure variation over the flat base of one of the after-burners. The model contained no sustainer rocket motor.

Model C

The constructional and geometrical characteristics of model C were essentially the same as model B with the exception of the horizontal stabilizer which was fixed at a deflection of -0.4° to trim model C at a low positive lift coefficient. The model was disturbed laterally by six small rockets, mounted in the nose, whose thrust produced a short lateral acceleration. The timing of these pulses placed two of them in the supersonic speed range and the remainder in the transonic and high subsonic ranges.

The geometric and mass characteristics of models A, B, and C are given in tables II and III, respectively.

Models D, E, and F

Models D, E, and F consisted of 10-percent-scaled reproductions of the assumed full-scale airplane wing mounted on pointed cylindrical bodies 9 inches in diameter with a cruciform arrangement of delta tail fins. The basic model wings (not including wing fillet area which is achieved by a trailing-edge chord-extension at the root) had an aspect ratio of 4.281 and a taper ratio of 0.284 and were swept back 36.840 at the 20-percent-chord line. A photograph of one of the models and a dimensioned sketch are shown in figures 7 and 8, respectively.

The models were tested with a fixed aileron deflection. The wing of model D was of very stiff construction with an aileron deflection of 25°. The wings of models E and F, on which the ailerons were deflected 15° and 25°, respectively, approximated the scaled-down stiffness characteristics of the full-scale airplane wing.



INSTRUMENTATION

A telemeter which transmitted time histories of the primary data as the models traversed the Mach number range was installed in models A, B, and C. For models D, E, and F spinsondes were used to obtain the primary data, which were rolling velocity.

A rawinsonde released at the time of firing recorded the free-stream temperature and static pressure over the altitude range covered by each test. The velocity and position in space of the models were determined by a CW Doppler radar set and a radar tracking unit.

TESTS

Simulator Ground Tests

Three static firings of the sustainer motor for model A were made, and thrust, chamber pressure, and exit static pressure were measured. These tests were used to show that proper simulation would be achieved; they also served to calibrate the variation of exit-static pressure with chamber pressure. This calibration enabled calculation of thrust in flight.

Flight Tests

Flight tests of the models were conducted at the Langley Pilotless Aircraft Research Station at Wallops Island, Va. The models were accelerated to their maximum Mach numbers, which corresponded to about M=2.0 for models A, B, and C and about M=1.2 for models D, E, and F, by means of booster rocket motors which separated upon cessation of thrusting. A photograph of model B prior to launching is shown as figure 9. The Reynolds number range covered by the tests is given in figure 10. The data presented herein were obtained during the coasting phase of flight, with the exception of model A for which power-on data were obtained at M=1.5. The ratio of jet static pressure to freestream static pressure for the power-on portion of the flight varied from 3.5 to 4.0 as shown in figure 11.



ANALYSIS

Longitudinal Stability

Free oscillations of model B were created by pulsing the horizontal tail in an approximate square-wave motion which resulted in changes in normal acceleration, angle of attack, and hinge moment. The longitudinal-stability analysis of these oscillations is based on two degrees of freedom in pitch. The basic equations of motion used in the analysis are as follows:

$$Vm(\dot{\theta} - \dot{\alpha}) = (C_{L_{\alpha}}\alpha + C_{L_{\delta}}\delta) qS$$

$$\mathbf{I}_{\mathbf{Y}} \overset{\bullet}{\boldsymbol{\theta}} = \left(\mathbf{C}_{\mathbf{m}_{\alpha}} \boldsymbol{\alpha} + \mathbf{C}_{\mathbf{m}_{\dot{\alpha}}} \frac{\ddot{\mathbf{c}}}{2V} \overset{\bullet}{\boldsymbol{\alpha}} + \mathbf{C}_{\mathbf{m}_{\mathbf{q}}} \frac{\ddot{\mathbf{c}}}{2V} \overset{\bullet}{\boldsymbol{\theta}} + \mathbf{C}_{\mathbf{m}_{\delta}} \boldsymbol{\delta} \right) \mathbf{q} \mathbf{S} \ddot{\mathbf{c}}$$

In order to simplify the analysis and to permit the determination of equations for the more important aerodynamic derivatives a number of assumptions are necessary. It is assumed that during the time interval over which each calculation is made the following conditions exist: The forward velocity is constant and the aerodynamic forces and moments vary linearly with the variables α , δ , and θ . In the appendixes of references 2 and 3 can be found a more detailed discussion of the methods used in reducing the data from a flight time history to the parameters presented in this paper and the assumptions made in and the limitations of the test technique.

Some of the control characteristics and damping data obtained from this test are incomplete between Mach numbers of 0.80 and 1.07 because the conditions of damped oscillations and linear variation of aerodynamic forces and moments with angle of attack discussed in references 2 and 3 are not satisfied in this speed range.

Corrections for model pitching and yawing velocities by the method described in reference 4 were made to the air-flow indicators to obtain angles of attack and angles of sideslip. All coefficients, with the exception of hinge moments (which were based on the total horizontal-tail area) and pressure coefficients, were computed based on the theoretical wing area (fillet area excluded), and all angles were measured relative to the fuselage reference line. (See fig. 1.)

The total pitching-moment coefficients were calculated by the following equations:

$$\mathbf{C}_{m} \; = \; \frac{\mathbf{I}_{\underline{Y}} \ddot{\boldsymbol{\theta}}}{\mathbf{q} \mathbf{S}_{W} \ddot{\mathbf{c}}_{W}} \; - \left[\left(\mathbf{C}_{m_{\underline{\mathbf{q}}}} \; + \; \mathbf{C}_{m_{\underline{\mathbf{q}}}} \right) \dot{\boldsymbol{\alpha}} \right] \frac{\mathbf{\bar{c}}}{\mathbf{2} \mathbf{V}} \; - \; \left(\; \mathbf{C}_{m_{\underline{\mathbf{q}}}} \dot{\boldsymbol{\gamma}} \right) \frac{\mathbf{\bar{c}}}{\mathbf{2} \mathbf{V}}$$

The angular acceleration in pitch was obtained from the following relation:

$$\ddot{\theta} = \frac{d\dot{\theta}}{dt} = \frac{d(\dot{\gamma} + \dot{\alpha})}{dt}$$

The quantity $\dot{\alpha}$ was obtained by differentiating the measured α curve and the quantity $\dot{\gamma}$ was calculated from the measured accelerations at the model center of gravity.

A choking section and a total-pressure rake installed in the duct exit made it possible to determine mass-flow ratio and internal drag based on free-stream and duct-exit conditions. (See ref. 5.) The internal drag presented herein was calculated in the following manner:

$$C_{D,i} = \frac{1}{qS_W} \left[w(V - V_{exit}) - A_{exit} (p_{exit} - p_o) \right]$$

Calibration of the variation of exit static pressure with chamber pressure in static tests enabled calculation of the thrust in flight by use of the following equation:

$$F = p_e A_e \left(\gamma_e M_e^2 + 1 \right) - p_o A_e$$

Comparison of the vacuum impulse (the first term of the preceding equation integrated over the burning time) in the static tests with that in flight indicated a total impulse of approximately 10 percent more in flight. The impulse variation in three static tests was less than 3 percent; thus, an adjustment of the flight chamber pressure data was indicated. The measured chamber pressure was proportionally adjusted and the resulting thrust used in conjunction with the accelerometer measurements to determine the power-on drag coefficient. The power-on lift coefficients were also corrected to a zero thrust condition.

Lateral Stability

Throughout the test, model C executed a continuous lateral motion which showed little damping; thus the time to damp to one-half amplitude was considered infinite. Oscillations of small amplitudes were also

present in the traces of angle-of-attack and lift coefficient, which indicated inertia coupling between longitudinal and lateral motions. Although the effects of the lateral motion on the longitudinal motion were important in producing or modifying the longitudinal motion, the longitudinal motion produced a secondary effect on the lateral motion which was within the accuracy of the lateral stability measurements. On this basis the computations were based on the following equations for three degrees of freedom:

Side force:

$$\frac{mV}{qS}\left(\beta + r - \alpha p\right) - C_{Y} = 0$$

Rolling moment:

$$\frac{I_{X}}{qSb} \dot{p} - \frac{I_{XZ}}{qSb} r - C_{l_{\beta}} \beta - C_{l_{p}} \frac{pb}{2V} - \left(C_{l_{r}} - C_{l_{\dot{\beta}}}\right) \frac{rb}{2V} = 0$$

Yawing moment:

$$\frac{\mathbf{I}_{Z}}{qSb} \ \dot{\mathbf{r}} \ - \frac{\mathbf{I}_{XZ}}{qSb} \ \dot{\mathbf{p}} \ - \ \mathbf{C}_{n_{\beta}} \boldsymbol{\beta} \ - \ \mathbf{C}_{n_{p}} \ \frac{pb}{2V} \ - \ \left(\mathbf{C}_{n_{r}} \ - \ \mathbf{C}_{n_{\dot{\beta}}}\right) \frac{rb}{2V} = 0$$

In the side-force equation the gravity terms $\frac{W}{qS}(\phi \cos \theta + \psi \sin \theta)$

have been omitted. This assumption is valid for rocket-propelled models since the models have low wing loadings and are flown through rather dense air at high speeds so that the values of the gravity terms are very small. Also, in the lateral-force equation all the aerodynamic terms are combined into one term referred to as $C_{\rm V}$ or the total lateral force. This assump-

tion is valid since the total lateral force was measured by a transverse accelerometer and includes the contributions of rolling angular velocity, yawing angular velocity, and sideslip angle. It was further assumed that $^{C}_{Y}$ was equal to $^{C}_{Y}{}_{\beta}$. In the rolling-moment and yawing-moment equa-

tions, the assumption has been made that $\mathring{\beta}$ = -r in order that the yawing- and sideslipping-velocity derivatives may be combined to reduce the number of unknown aerodynamic terms.

The lateral equations of motion written in the form to analyze the data by the vector method are given in figure 12. More detailed discussions of the application of the time vector may be found in references 6, 7, and 8. The time vectors, such as the example given in figure 12 for one solution, constitute a three-degree-of-freedom analysis by using basic motional information such as the representative curves of the variation of side-force coefficient with angle of sideslip. The primary vectorial



data necessary for the analysis and obtained from the flight time history are as follows: the Dutch roll frequency, the damping factor, the undamped natural circular frequency, the phase difference between the roll rate and the angle-of-sideslip oscillations, and the amplitude ratio of the rate of roll to angle of sideslip. The phase angles include corrections required by the frequency response characteristics of the roll rate gyro.

The method allows the determination of two derivatives in each degree of freedom, whereas the third must be otherwise determined. The cross derivatives c_1 and c_n were assigned two values to show the effect

of selecting them as the derivatives not found in the analysis. A more complete discussion on the evaluation of this test technique is given in reference 8.

The frequency of the Dutch roll motion was also used to compute C by the following equation, which was written for one degree of freedom in yaw:

$$c_{n_{\beta}} = \frac{I_{Z}}{qSb} \omega^{2}$$

and the difference in $C_{n_{\beta}}$ shown by the two methods is a measure of the effect of neglecting the product of inertia terms. The inclination of the principal axis, measured to be -4.2°, was used to compute the product of inertia.

ACCURACY

The estimated probable errors in the basic quantities measured are shown in table IV. The stability derivatives presented in this paper are dependent upon some or all of these measured quantities. An analysis by the methods of references 6 and 8 of the probable errors in some of the derivatives due to the probable errors quoted in table IV indicates the following errors at M = 1.7 and M = 0.85:

																										number 0.85
$^{\mathrm{C}}_{\mathrm{L}}$,	percent	•	•	•	•	•		•	•	•	•		•	•	•	•	•	•	•	•	•	•	•	•	±2	± 5
C_{D} ,	percent		•	•	•	•	•	•	•	•	•	•	•	•	•	•	•	•	•	•	•	•	•		±2.5	±7



		number 0.85
Cy, percent	• ±3	±5
$C_{n_{\beta}}$ and $C_{l_{\beta}}$, percent	• ±5	±8
C _{ln} , percent	. ±14	±17
$C_{n_r}^{P} - C_{n_{\beta}^{\bullet}}$, percent	• ±15	±25

The pb/2V data for models D, E, and F have not been corrected for the effects of rolling moment of inertia. Reference 9 shows this correction to be small except in the transonic region, where rolling accelerations become large. For this reason, the accuracy limits in the transonic region (0.88 < M < 1.00) are about ± 20 percent, whereas at subsonic and supersonic speeds the accuracy is about ± 10 percent.

Base- and internal-drag data were obtained from pressure measurements and therefore have different possible errors than the drag values based on acceleration measurements. The maximum possible errors in both of these quantities due to instrument inaccuracy would be so small that they would not change any three-decimal-place drag values used.

It is believed that the data presented in this report provide a good indication of the variation of the stability derivatives with Mach number and the absolute values of these derivatives are at least as accurate or better than indicated above.

RESULTS AND DISCUSSION

Lift and Trim Characteristics

Lift.- Coefficients are based on total wing area, excluding wing fillet area, as shown in figure 1. Lift characteristics as a function of angle of attack for some representative Mach numbers are given in figure 13(a). These values of C_L represent the range covered at the indicated Mach numbers. The variation of C_L with α is essentially linear over the C_L and M range covered by the tests with the exception of M = 0.86 where an abrupt break occurs at $C_L = 0.75$. Values of lift-curve slope C_L taken over the linear portion of these plots are presented in figure 13(b).

The power-on and power-off values of $C_{L_{\alpha}}$ obtained from model A in addition to unpublished tunnel results are presented for comparative purposes with the results obtained from model B. Data presenting the variation of C_L with α from model A are limited in both lift range covered and quantity since the primary purpose of the investigation was to determine the effect of the engine jet exhaust on the drag and trim characteristics of the configuration. The data from model A indicate that there might have been some reduction in power-off $C_{L_{\alpha}}$ due to fairing over the inlets; however, in general, the agreement between the three sources is considered good. There are no unusual variations or trends in lift-curve slope over the Mach number range covered.

The flight time history of normal acceleration showed the presence of high-frequency oscillations as the model pitched to the higher lift coefficients below M = 0.93. These oscillations are believed to represent the buffet-intensity rise, which occurred at about $C_{\rm L}$ = 0.59 at M = 0.93 and $C_{\rm L}$ = 0.65 at M = 0.86 with the maximum amplitude being $\Delta C_{\rm L} \approx$ 0.1. As a result of the high frequency of the oscillations (115 cps) and since obtaining buffet information was not a primary purpose of this test, the minimum amplitude of $\Delta C_{\rm L}$ which can be obtained from the instrumentation used is 0.03.

Trim. - The effect of power on the trim-lift coefficient and angle of attack is shown in figure 14. The measured trim angle of attack with respect to the fuselage reference line is presented for both the power-on and the power-off portions of the flight. The values of power-on trimlift coefficient were obtained by correcting the measured-lift coefficients for the thrust component along the lift axis. Power-on produced a decrease in trim angle of attack of approximately 1.1° and a trim-liftcoefficient decrease of about 0.06 at a Mach number of about 1.5. The model thrust axis was below the center of gravity producing a pitch-up moment, thus alleviating to some extent the pitch-down effect induced by the jet exhaust. With the thrust axis through the center of gravity the model change in trim with power on would have been slightly greater. The decrease in trim angle of attack corrected to thrust through the center of gravity was approximately 1.27° with a decrease in trim-lift coefficient of approximately 0.072. During power-on, burning of the propellant caused a gradual shift in the center-of-gravity location. The power-off data for the rest of the flight are for a center-of-gravity location of 17.8 percent c.

The jet-off pressure coefficients for the various orifice locations shown in figure 4 are presented in figure 15. The discontinuity and temporary increase in several of the coefficients at a Mach number of about 1.5 are believed to have been caused by intermittent burning of

propellant remnants. Orifice number 8 (horizontal stabilizer) is omitted at high Mach numbers due to the fact that this pressure varied with angle of attack and since it was measured intermittently it was impossible to get a complete time history. None of the other pressures appeared to be influenced by changes in angle of attack encountered.

Figure 16 shows the incremental change in pressure coefficient caused by the jet exhaust ($\Delta C_p = C_p$,power-on - C_p ,power-off) for the power-on portion of the flight. Measurements prior to power-on were used for C_p ,power-off. In figure 16(a) a general increase in pressure along the bottom of the fuselage is indicated with the most forward orifice showing little change and the most rearward orifice showing the greatest increase.

Pressure coefficients on the side of the fuselage (fig. 16(b)) indicated that power-on caused an increase near the jet and a gradual decrease to a high negative change approximately two jet diameters to the rear of the jet exit. The base annulus pressures were increased considerably but the portion of the annulus inboard showed about 35 percent less increase than the outboard portion of the annulus (fig. 16(c)). This effect is believed to be caused by the influence of the fuselage—tail-pipe juncture in the vicinity of the base. Power-on produced an approximate change in pressure coefficient ΔC_p = 0.11 for orifice number 8 (horizontal stabilizer) but it is not possible to determine what the change would have been with no angle-of-attack change. The small range of the ratio of jet-exit static pressure to free-stream static pressure (fig. 11) encountered in flight precludes the determination of the effect of pressure ratio on any of the data presented; however, it is noted that several of the incremental changes follow the same trend as the pressure ratio.

Drag

Basic drag. The basic drag data from model B are presented in the form of lift-drag curves in figure 17. These curves are for various Mach numbers and lift ranges and the drag values include both internal and base drag. The mass-flow ratios at which the tests were conducted are given in figure 18.

Minimum drag. The variations of the lift coefficient for minimum drag, $(CL)C_{D,min}$ and the minimum-drag coefficient $C_{D,min}$ as determined from the lift-drag curves of figure 17 are presented as a function of Mach number in figures 19 and 20. The values of $C_{D,min}$ include both internal and base drag. Values of $C_{D,i}$ and $C_{D,b}$ are also presented in figure 20. At the higher horizontal-tail deflections the model did not oscillate to minimum drag.

Between M = 0.82 and M = 0.87, $C_{D,min}$ is constant at about 0.020. The drag rise occurs at M = 0.90 (the Mach number at which $\frac{dC_D}{dM}$ = 0.10) and at M = 1.10, $C_{D,min}$ has a value of 0.070. The drag continues to increase gradually with Mach number and at M = 1.83 has a value of $C_{D,min}$ = 0.074.

Base drag. - The base-drag data were obtained from the base-pressure survey taken on the exit of the afterburner on model B. The base-drag coefficient varied from about 0.001 at subsonic speeds to about 0.002 at supersonic speeds.

Internal drag. The values of internal-drag coefficient determined from model B and presented in figure 20 are nearly a constant value of 0.005 from M = 1.01 to M = 1.84. No subsonic values could be obtained since the duct became unchoked below M = 1.0; however, other tests have shown the internal-drag level remains about the same at subsonic and supersonic speeds for cases where the variation in mass-flow ratio is small.

Jet effects on drag.— The variation of power-on and power-off drag coefficients with time at $C_{\rm L}$ = 0.11 is shown in figure 21. The power-off data were obtained just previous to simulator firing and cannot be directly compared with the drag data discussed from model B in the preceding paragraphs since the inlets were faired over on model A. The power-off data presented in figure 21 are corrected to zero base drag, and during power-on the base-drag coefficient was negligible. This drag comparison is not the difference in the airplane drag power-off and power-on, but shows the effect of the jet exhaust on the external drag. The power-off total-drag coefficient would be greater by the base-drag coefficient and also would involve a change in inlet drag from a low inlet drag at maximum mass flow to a high inlet drag at zero mass flow.

The data indicate that the power-on drag coefficient is equal to or as much as 10 percent less than the power-off drag coefficient. This variation is believed to be due to inaccuracies in the determination of thrust. The average power-on drag is less than power-off, but the increment is within the accuracy of the data.

Longitudinal Stability

Static.- The static-longitudinal-stability characteristics of the configuration with open ducts, model B, are shown in figures 22 to 24. All moment data were taken about the center-of-gravity location at $0.169\bar{c}$.

Some representative curves of pitching-moment coefficient C_m as a function of C_L for various tail deflections and Mach numbers are presented in figure 22. At Mach numbers above 1.09 the curves presented in figure 22(a) are linear for the C_L range covered; however, at M=1.09 there is a slight change in pitching-moment slope at $C_L=0.05$. Figure 22(b) shows that at M=0.94 and M=0.95 there is a change in slope beginning at $C_L=0.10$. The curve at M=0.85 shows an almost linear variation of C_m with C_L in the lift range from $C_L=0.56$ to the point where an abrupt change in slope occurs at $C_L=0.83$. These pitching-moment curves at the subsonic Mach numbers, where a large lift range was covered, indicates a reduction in stability at the higher lift coefficients. The measured periods P of the short-period longitudinal oscillations resulting from the abrupt control movement are given in figure 23. These values were used to calculate the longitudinal stability parameter $C_{m_{\alpha}}$ by the following relation:

$$C_{m_{CL}} = -\frac{I_{Y}}{qS_{W}\bar{c}_{W}} \left[\frac{h_{\pi}^{2}}{p^{2}} + \left(\frac{0.693}{t_{1/2}} \right)^{2} \right]$$

The values of $C_{m_{\alpha}}$ in conjunction with $C_{L_{\alpha}}$ were used to compute aerodynamic-center values for comparison with those obtained from the slopes of the pitching-moment curves which are shown in figure 24. The slopes of the pitching-moment curves were taken over the linear portion of the curves (fig. 22). The aerodynamic center moved from a location of 62 percent mean aerodynamic chord at M = 0.88 to its most rearward location of 85 percent mean aerodynamic chord at about M = 1.40 and then decreased to a value of 81 percent mean aerodynamic chord at M = 1.72.

The aerodynamic-center location was obtained at several isolated times from the flight time history of model A. These data are plotted in figure 24 for comparison. The data in general show good agreement with those from model B, but because of the scatter of the data it is felt that the effect of the jet exhaust on the center of pressure should not be interpreted from these data.

Basic pitching moment.— The basic pitching-moment coefficient C_{m_O} at zero tail deflection and zero angle of attack is shown in figure 25. The wing of the model had 1^O of positive incidence relative to the model center line, which was used as the reference in this test. Since most of the tunnel data used the wing as the reference, figure 25 shows C_{m_O} computed by using $\alpha = 0^O$ relative to the wing as well as to the model center line. Unpublished wind-tunnel data are plotted for comparison

and the agreement is good at supersonic speeds. A value of C_{m_O} was computed at M = 0.88 by using rocket-model values of $C_{m_{C_L}}$ and C_{L_C} and unpublished wind-tunnel values of control effectiveness. The agreement between this value of C_{m_O} and the tunnel value at M = 0.90 is good.

Values of C_{m_0} calculated for 0° wing angle of attack vary from 0.076 at M = 1.06 to 0.048 at M = 1.77.

Damping in pitch. The damping-in-pitch characteristics are given by the parameters $t_{1/2}$ and $C_{m_{\mbox{\scriptsize q}}}+C_{m_{\mbox{\scriptsize d}}}$ which are presented in figures 26 and 27, respectively. These parameters were determined from an analysis of the rate of decay of the transient short-period oscillations resulting from abrupt horizontal-tail movements. Figure 27 shows a decrease in pitch damping between M = 0.90 and 1.02 followed by a gradual increase to M = 1.40 and a more rapid increase between M = 1.40 and M = 1.75. Pitch-damping data from the rocket test of a model having a horizontal tail of aspect ratio 4.33 (ref. 10) show the same general variation of $C_{m_{\mbox{\scriptsize q}}}+C_{m_{\mbox{\scriptsize d}}}$ with Mach number. The configuration tested in this investigation was dynamically stable without any unusually large reductions in damping in pitch over the speed range covered.

The horizontal stabilizer, however, did not remain at a fixed angle but oscillated about a mean trim line in phase with α as a result of the high hinge moments at supersonic speeds. The maximum $\Delta\delta$ of this oscillation was in the order of 0.5° with an average value of about 0.25°. The static derivatives were corrected for this effect; however, no dynamic corrections were made for this effect.

Longitudinal control effectiveness.— The effectiveness of the all-movable horizontal tail of aspect ratio 3.30 in producing lift and pitching moments is given in figures 28 and 29. The lift coefficient per degree of tail deflection $C_{L_{\delta}}$ has a value of 0.0105 at about M=1.05 and decreases gradually with increase in Mach number until at M=1.70 the value of $C_{L_{\delta}}$ is 0.0070. Pitching-moment effectiveness $C_{m_{\delta}}$ varies from -0.036 at M=1.00 to a value of -0.023 at M=1.70.

Two other longitudinal-control effectiveness parameters, the change in trim angle of attack per degree of tail deflection $\Delta\alpha/\Delta\delta$ and the rate of change in trim-lift coefficient with tail deflection $\Delta C_L/\Delta\delta$, are presented as functions of Mach number in figures 30 and 31, respectively.

The horizontal tail is an effective pitch control throughout the Mach number range covered. All the effectiveness parameters show gradual variations with Mach number.

Hinge moments.— The hinge-moment characteristics of the horizontal tail in the form of the variation of hinge-moment coefficient with angle of attack C_{h_α} and the variation of hinge-moment coefficient with tail deflection C_{h_δ} are given in figures 32 and 33. The parameter C_{h_α} was obtained from the linear portion of plots of C_h against α (approximately 0° to 4°) and C_{h_δ} was determined by the method discussed in reference 2. The horizontal tail was hinged at 26.5 percent of the tail mean aerodynamic chord and had an unswept hinge line. Figure 32 shows that C_{h_α} varies from a value of 0.0020 at M = 0.82 to C_{h_α} = -0.0075 at M = 1.55 and at M = 1.72 had a value of -0.0055. Figure 33 shows a steady decrease in C_{h_δ} from -0.0170 at M = 1.07 to C_{h_δ} = -0.0073 at M = 1.70.

Lateral Stability

The lateral derivatives obtained from model C, with the exception of the rolling-effectiveness parameter pb/2V, are all presented as groups of data points. The results give a visual estimation of the accuracy of determining each derivative. Also shown are the effects of neglecting the cross derivatives and the product-of-inertia terms, as explained in the "Analysis" section. Two sections of the time history which show some of the quantities measured and the lack of damping of the β oscillation are shown in figure 34. The vectorial data necessary to obtain the lateral stability derivatives by the time-vector method are presented in the following figures: variation of side-force coefficient with angle of sideslip at various Mach numbers (figs. 35 and 36), the Dutch roll frequency (fig. 37), the phase difference between the roll rate and the angle-of-sideslip oscillations and between the side-force coefficient and the angle-of-sideslip oscillations (fig. 38), and the amplitude ratio of the rate of roll to angle of sideslip (fig. 39).

Static.- The dihedral-effect derivative $c_{l_{\beta}}$ (fig. 40) shows little change in value with change of c_{l_r} and indicates the dihedral effect was adequate.

The static lateral stability $c_{n_{\beta}}$ (fig. 41) is shown for the two methods of computation and for the change in c_{n_p} . The values of $c_{n_{\beta}}$ based on a one-degree-of-freedom analysis of the periods are slightly

different from those found by the vector computations. The difference is a measure of the effect of neglecting the product-of-inertia terms. The change in C_{n_0} has a negligible effect on $\text{C}_{n_\beta} \bullet$

<u>Dynamic.</u> The roll-damping derivative C_{lp} is presented in figure 42, where the apparent scatter is mainly a result of the variation of Ω_p in figure 38. Theoretical values are shown as computed from references 11 and 12. The roll damping remained near the same level throughout the speed range and agreed with the theoretical values.

Presented in figure 43 is the dynamic-lateral-stability derivative C_{n_T} - $C_{n_{\dot{\beta}}}$ which shows a greater effect of the change in C_{n_p} . The derivative C_{n_T} - $C_{n_{\dot{\beta}}}$ remains negative throughout the speed range, but the model motion showed little damping. The reason for little or no damping observed in the model motion was the result of large roll coupling due to the relatively large product of inertia. For the angle of attack of this test the out-of-phase yawing moment contributed by the product-of-inertia term is of opposite sign and larger magnitude than that contributed by C_{n_T} - $C_{n_{\dot{\beta}}}$ (see fig. 12).

Effect of aeroelasticity on pb/2V.- The stiffness characteristics of the wings of models D, E, and F are compared with the scaled-down stiffness characteristics of the assumed full-scale airplane wing in figure 44.

The variation of the rolling-effectiveness parameter pb/2V with Mach number is shown in figure 45. These pb/2V values have been corrected by the method of reference 13 for the small wing and tail incidence angles resulting from construction tolerances. Included in figure 45 is the rigid-wing rolling effectiveness which was estimated by cross plotting the data for 25° aileron deflection against θ'/m' and making a straight line extrapolation to $\theta'/m' = 0$.

Flexible-wing rolling effectiveness at sea level and 35,000 feet was estimated from the data for 25° aileron deflection by assuming that the loss in rolling effectiveness $1 - \emptyset'$ is proportional to the dynamic pressure q. The variation of $1 - \emptyset'$ and q with Mach number for the flexible-wing model with 25° aileron deflection at test altitudes is shown in figure 46. Estimated flexible-wing rolling effectiveness at sea level and 35,000 feet is compared with estimated rigid-wing rolling effectiveness in figure 47. Figure 47 shows that the loss in rolling effectiveness due to aeroelasticity varied from about 6 percent at 35,000 feet to about 27 percent at sea level at a Mach number of 0.5 and from about 20 percent at 35,000 feet to about 84 percent at sea level at a Mach number of 1.2.

CONCLUSIONS

Results from the flight tests of models of a fighter-type airplane in the Mach number M range from 0.5 to 1.9 indicate the following conclusions:

- 1. The jet-engine simulator caused a decrease in trim angle of attack of approximately 1.27° and a decrease in trim-lift coefficient of 0.07.
- 2. The pressure coefficient for the base annulus was increased, but the increase was smaller on the portion of the annulus adjacent to the fuselage.
- 3. Pressure coefficients on the side and bottom of the fuselage indicated a positive increment near the jet exit. As the distance downstream of the jet exit increased, the increment on the bottom of the fuselage increased, whereas the increments on the side decreased to a negative peak.
- 4. The drag rise begins at M = 0.90. The minimum-drag coefficient (including base and internal drag) has a value of 0.02 at M = 0.87, an increase to 0.070 at M = 1.1, and then a gradual increase to a value of 0.074 at M = 1.83.
- 5. The static longitudinal stability is reduced at the higher lift coefficients at subsonic speeds.
- 6. The aerodynamic-center location is at 62.0 percent mean aerodynamic chord at M = 0.88 and reaches its most rearward position of 85.0 percent mean aerodynamic chord at M = 1.4.
- 7. The pitch-damping parameters indicated that the configuration possessed dynamic longitudinal stability without any unusually large reductions over the speed range covered.
- 8. Variation of horizontal-tail effectiveness with Mach number from 1.00 to 1.70 was gradual and the tail remained an effective control for producing forces and moments throughout the speed range.
- 9. The pitching-moment coefficient at 0° wing angle of attack and 0° tail deflection decreases from a positive value of 0.076 at a Mach number of 1.06 to 0.048 at a Mach number of 1.77.
- 10. The roll damping remained near the same level throughout the speed range tested and agreed well with some theoretical values.
 - 11. There was an adequate dihedral effect.

- 12. The cross derivatives c_{n_p} and c_{l_r} were not determined, but their effects on the other derivatives were shown to be small.
- 13. The loss in rolling effectiveness due to aeroelasticity varied from about 6 percent at 35,000 feet to about 27 percent at sea level at M=0.5 and from about 20 percent at 35,000 feet to about 84 percent at sea level at M=1.2.

Langley Aeronautical Laboratory,
National Advisory Committee for Aeronautics,
Langley Field, Va., October 31, 1956.



REFERENCES

- 1. DeMoraes, Carlos A., Hagginbothom, William K., Jr., and Falanga, Ralph A.: Design and Evaluation of a Turbojet Exhaust Simulator, Utilizing a Solid-Propellant Rocket Motor, for Use in Free Flight Aerodynamic Research Models. NACA RM L54I15, 1954.
- 2. Mitcham, Grady L., Stevens, Joseph E., and Norris, Harry P.: Aero-dynamic Characteristics and Flying Qualities of a Tailless Triangular-Wing Airplane Configuration As Obtained From Flights of Rocket-Propelled Models at Transonic and Low Supersonic Speeds. NACA TN 3753, 1956. (Supersedes NACA RM L9L07.)
- 3. Gillis, Clarence L., Peck, Robert F., and Vitale, A. James: Preliminary Results From a Free-Flight Investigation at Transonic and Supersonic Speeds of the Longitudinal Stability and Control Characteristics of an Airplane Configuration with a Thin Straight Wing of Aspect Ratio 3. NACA RM L9K25, 1950.
- 4. Ikard, Wallace L.: An Air-Flow-Direction Pickup Suitable for Telemetering Use on Pilotless Aircraft. NACA TN 3799, 1956. (Supersedes NACA RM L53Kl6.)
- 5. Faget, Maxime A., Watson, Raymond S., and Bartlett, Walter A., Jr.: Free-Jet Tests of a 6.5-Inch-Diameter Ram-Jet Engine at Mach Numbers of 1.81 and 2.00. NACA RM L50L06, 1951.
- 6. Mitchell, Jesse L., and Peck, Robert F.: Investigation of the Lateral Stability Characteristics of the Douglas X-3 Configuration at Mach Numbers From 0.6 to 1.1 by Means of a Rocket-Propelled Model. NACA RM 154L20, 1955.
- 7. D'Aiutolo, Charles T., and Henning, Allen B.: Lateral Stability Characteristics at Low Lift Between Mach Numbers of 0.85 and 1.15 of a Rocket-Propelled Model of a Supersonic Airplane Configuration Having a Tapered Wing With Circular-Arc Sections and 40° Sweepback. NACA RM L55A31, 1955.
- 8. Gillis, Clarence L., and Chapman, Rowe, Jr.: Effect of Wing Height and Dihedral on the Lateral Stability Characteristics at Low Lift of a 45° Swept-Wing Airplane Configuration As Obtained From Time-Vector Analyses of Rocket-Propelled-Model Flights at Mach Numbers From 0.7 to 1.3. NACA RM L56E17, 1956.
- 9. Sandahl, Carl A., and Marino, Alfred A.: Free-Flight Investigation of Control Effectiveness of Full-Span 0.2-Chord Plain Ailerons at High Subsonic, Transonic, and Supersonic Speeds To Determine Some Effects of Section Thickness and Wing Sweepback. NACA RM L7DO2, 1947.

- 10. Peck, Robert F., and Hollinger, James A.: A Rocket-Model Investigation of the Longitudinal Stability, Lift, and Drag Characteristics of the Douglas X-3 Configuration With Horizontal Tail of Aspect Ratio 4.33. NACA RM L53F19a, 1953.
- 11. Malvestuto, Frank S., Jr., Margolis, Kenneth, and Ribner, Herbert S.:
 Theoretical Lift and Damping in Roll at Supersonic Speeds of Thin
 Sweptback Tapered Wings With Streamwise Tips, Subsonic Leading Edges,
 and Supersonic Trailing Edges. NACA Rep. 970, 1950. (Supersedes
 NACA TN 1860.)
- 12. Martin, John C., and Jeffreys, Isabella: Span Load Distributions Resulting From Angle of Attack, Rolling, and Pitching for Tapered Sweptback Wings With Streamwise Tips Supersonic Leading and Trailing Edges. NACA TN 2643, 1952.
- 13. Strass, H. Kurt, and Marley, Edward T.: Rolling Effectiveness of All-Movable Wings at Small Angles of Incidence at Mach Numbers From 0.6 to 1.6. NACA RM L51H03, 1951.

TABLE I COMPARISON BETWEEN PERFORMANCES OF SIMULATOR

[Simulator performance corrected to full scale and altitude of 35,000 feet; all data for one engine]

AND PRATT & WHITNEY J57 TURBOJET ENGINE

	Rocket simulator	Turbojet design
Jet stagnation temperature, ^O F abs Specific heat ratio	4,000 1.25	3 , 200 1 . 27
stream static pressure Jet thrust, lb	6.3 to 7.2 15,200 to 15,900	7.10 15,600
Average jet gross weight flow, lb/sec	120	122
Jet exit area (afterburner condition), sq ft	3•99	3.98

TABLE II

PHYSICAL CHARACTERISTICS OF MODELS A, B, AND C

Wing:	
Area (theoretical), sq ft 5.75	5
Span, ft	7
Aspect ratio	8
Mean aerodynamic chord, ft	8
Taper ratio	8
Sweepback of leading edge, deg	
Sweepback of trailing edge, deg	2
Incidence angle (with respect to model center line), deg 1.00	
Dihedral angle, deg	_
aRoot thickness (theoretical), percent chord 6.6	_
^a Tip thickness, percent chord	
Tip thickness, percent chord	L
Horizontal tail:	
Total area, sq ft	7
Span, ft	7
Aspect ratio	
Mean aerodynamic chord, ft	
Taper ratio	5
Sweepback of leading edge, deg 39.80	
Sweepback of trailing edge, deg 20.93	
Dihedral angle, deg	
Root airfoil section NACA 65A007 (modified)	
Tip airfoil section NACA 65A006 (modified)	
Tail length (25 percent wing mean aerodynamic chord to	,
25 percent tail mean aerodynamic chord)	`
2) percent tail mean aerodynamic chord,	1
Fuselage:	
Length, ft	3
Width (maximum), ft 0.96	5
Height (maximum), ft 0.88	3
Maximum cross-sectional area, sq ft 0.66	
Ducts (one side):	
Inlet area, sq ft 0.0625	
Exit area, sq ft	ł
Area at compressor face (excluding area blocked	
by accessory housing), sq ft 0.0802	2
Vertical tail:	
Area above fuselage (dorsal excluded), sq ft 1.18)
Area above luserage (dorsar excluded), sq 1t	
Span, ft 0.94	
Mean aerodynamic chord (theoretical), ft 1.46	
Aspect ratio (theoretical) 0.66	
Sweepback angle at leading edge, deg	
Sweepback angle at trailing edge, deg 16.60	
Root airfoil section NACA 65A007	7
Tip airfoil section NACA 65A007	7

^aRoot and tip airfoil sections are NACA 65A007 and 65A006, respectively, modified by extending the chord 5 percent forward of the 16.04-percent-chord line and adding 1.67 percent positive camber.

bDucts were faired over on model A.

TABLE III
WEIGHT AND BALANCE DATA FOR MODELS A, B, AND C

Model	Weight,	Wing loading, lb/sq ft	Center-of-gravity position,		t of inertia, slug-ft ²						
	lb	TD/SQ 10	percent c	I_{X}	I _Y	I_{Z}					
	Rocket fuel included in model										
А	489.75	85.3	21.2		53.30						
	Models without rocket fuel										
A B a.C	455.81 405.25 379.40	79·3 70·5 66·0	17.80 16.90 17.30	 3.57	52.64 54.95 46.30	 47.78					

^aInclination of principal axis was -4.2°.

TABLE IV

ESTIMATED ACCURACIES OF VARIOUS MEASURED QUANTITIES

[All increments may be positive or negative]

Model	Overtity	Estimated accuracy at -						
Model	Quantity	M = 1.7	M = 0.85					
A, B, C D, E, F A, B, C D, E, F A, B, C B, C B, C B	M, percent M, percent q, percent q, percent W, percent IX, percent Iz, percent IXZ, percent IXZ, percent a, deg b, deg b, deg P, sec	1.0 2.0 .5 3.5 2.0 2.0 8.0 .5 .5 .2	2.5 1.0 5.0 5.0 3.5 2.0 2.0 8.0 .5 .5 .2					
C	$\left \frac{\mathbf{p}}{\mathbf{\beta}}\right $, percent	3.0	3.0					
С	$\left \frac{a_t/g}{\beta}\right $, percent	2.0	2.0					
C C	ω , percent $\Omega_{ m p}$, deg	2.5 3.0	2.5 3.0					

^aPrimarily due to estimated accuracy of principal axis inclination $(1/2^{\circ})$.

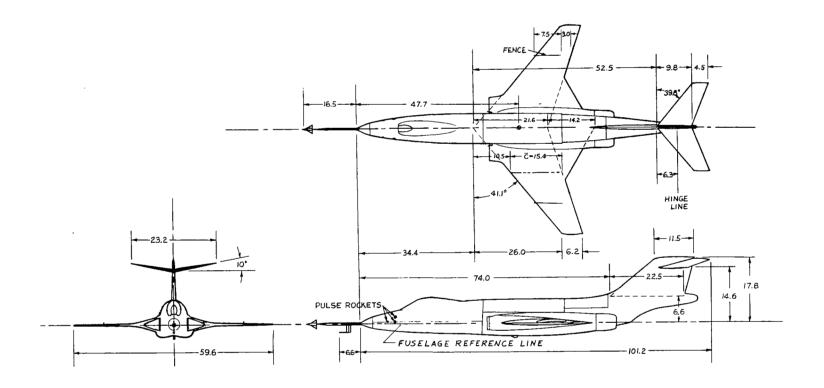


Figure 1.- Three-view drawing of models B and C. Model A is essentially similar except for wing root inlets, which were faired for installation of rocket-motor simulator. Broken lines indicate plan form of theoretical wing. All dimensions are in inches.

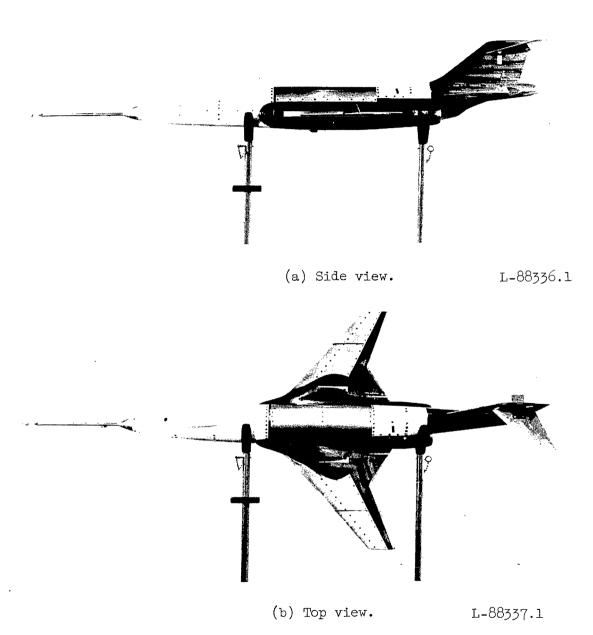


Figure 2.- Photographs of model A.

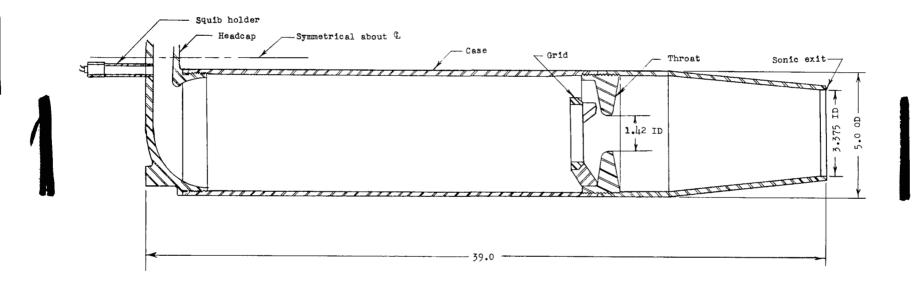


Figure 3.- Sketch of rocket simulator. All dimensions are in inches.

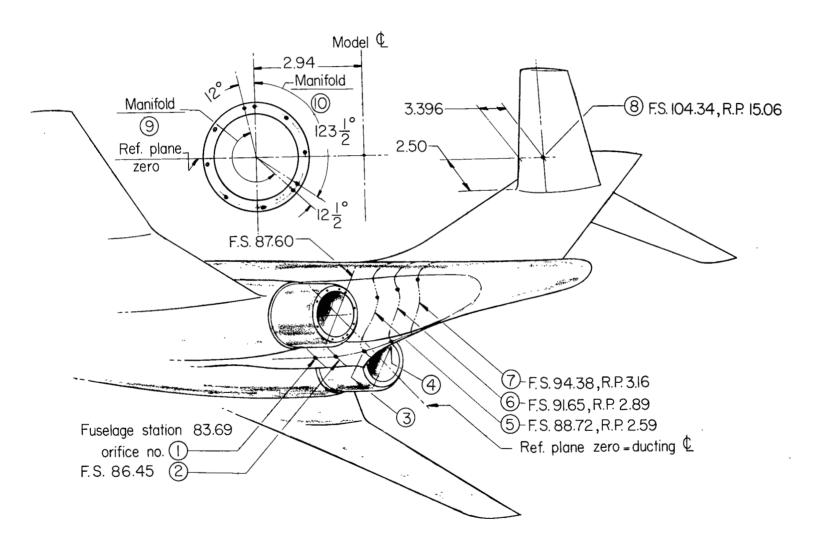
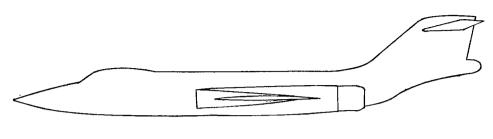


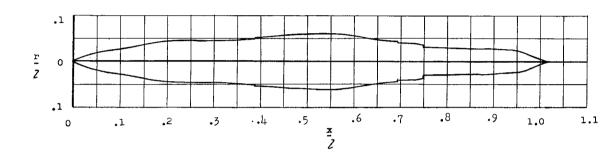
Figure 4.- Pictorial layout of orifice locations.

Figure 5.- Photograph of model B.

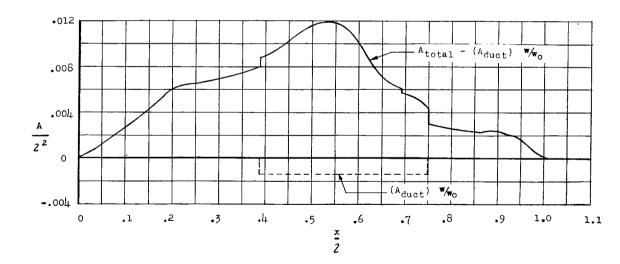
L-86586.1



Model



(a) Equivalent body of revolution.



(b) Area distribution.

Figure 6.- Area distribution and equivalent body of revolution of models B and C.

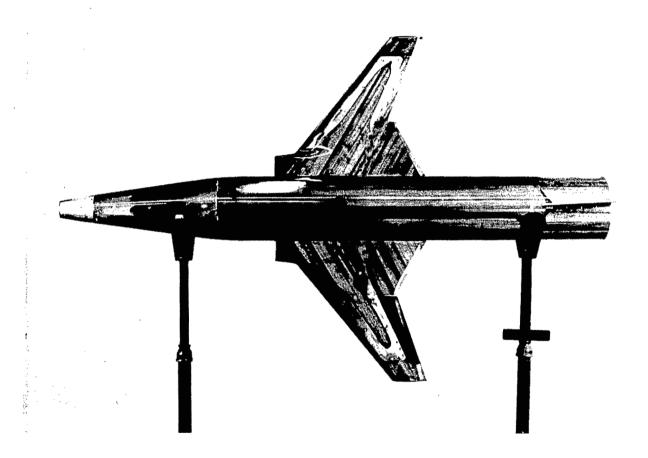


Figure 7.- Photograph of typical model D, E, and F. L-87108.1

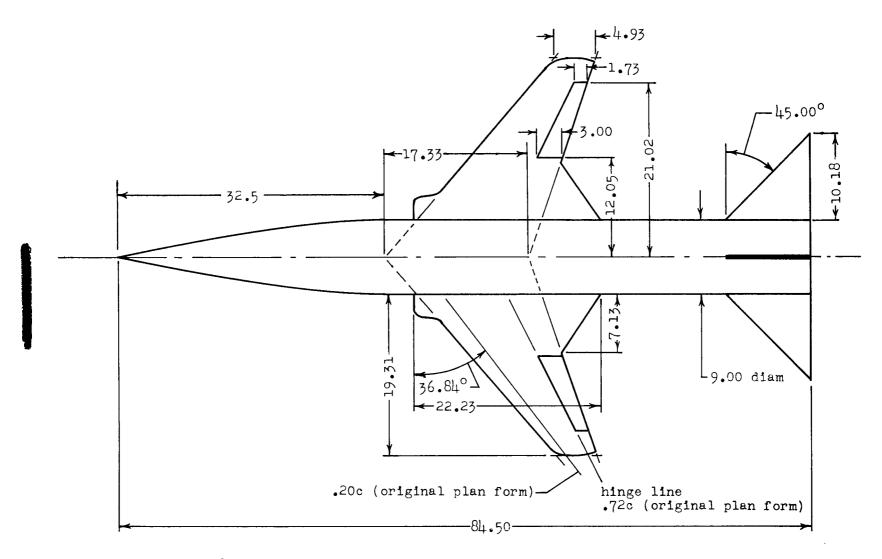
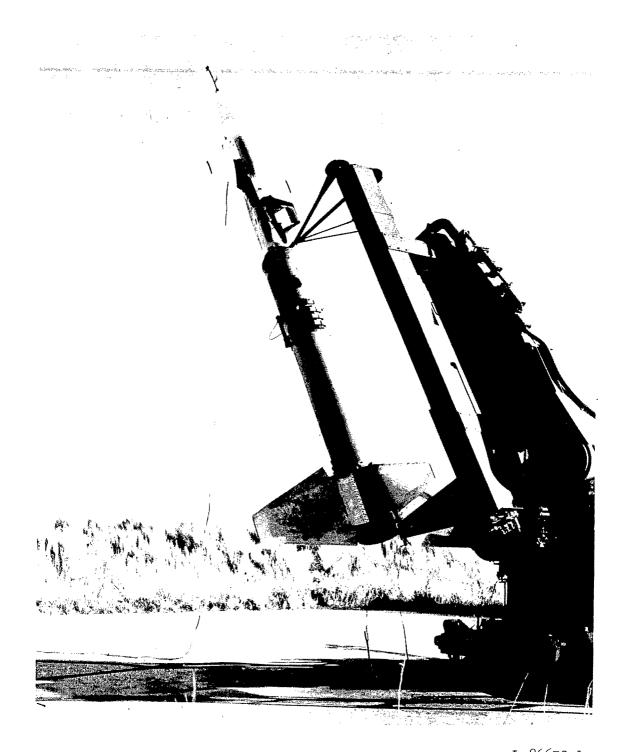


Figure 8.- Sketch of configurations D, E, and F. All dimensions are in inches.

NACA RM L56K19



\$L-86652.1\$ Figure 9.- Photograph of model-booster combination on launcher.

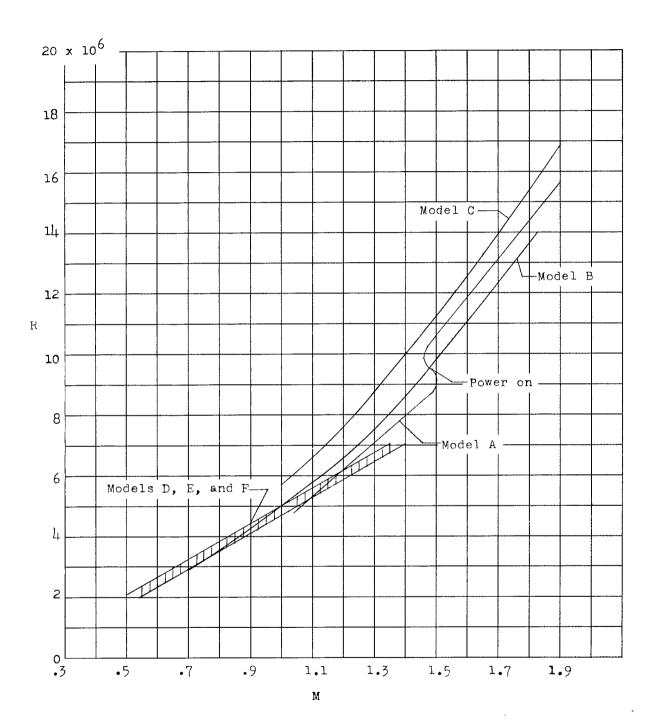


Figure 10.- Reynolds number variation with Mach number for all tests.

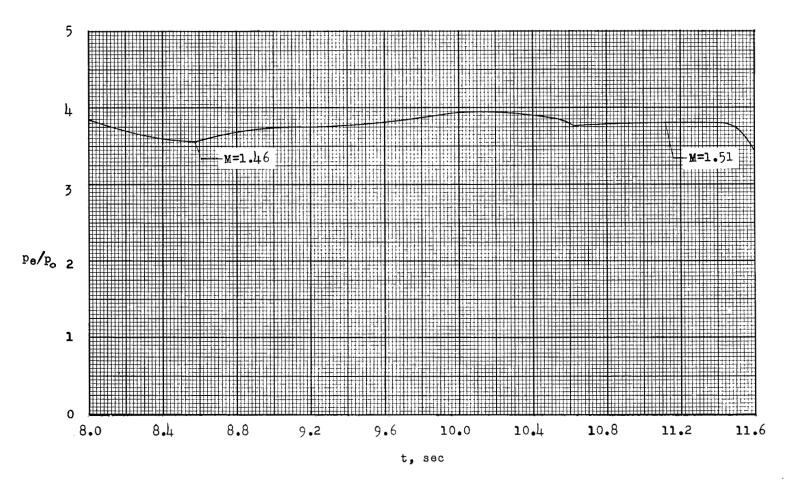
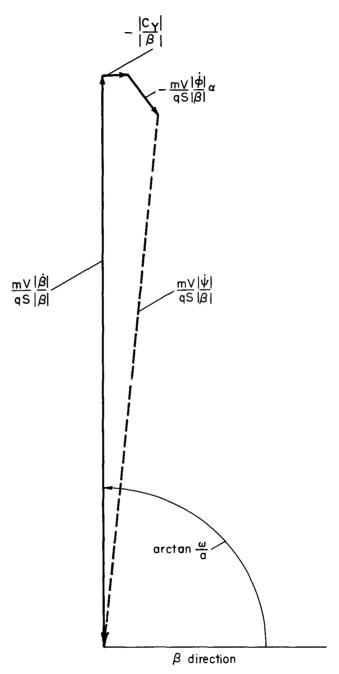


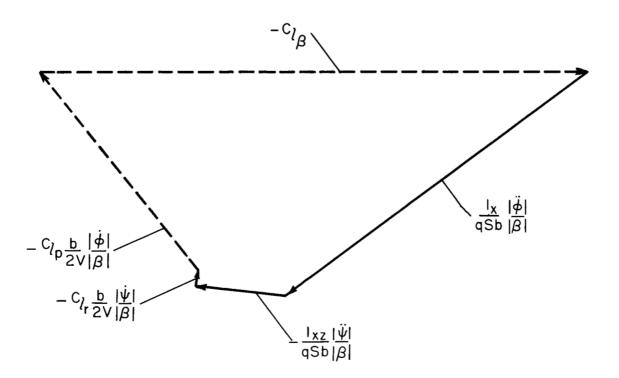
Figure 11.- Variation of ratio of jet-exit static pressure to free-stream static pressure with time for power-on portion of flight. Model A.



Sideforce equation:

$$\frac{m \vee |\dot{\beta}|}{q \, S \, |\dot{\beta}|} + \frac{m \vee}{q \, S} \, \frac{|\dot{\psi}|}{|\dot{\beta}|} - \frac{m \vee}{q \, S} \, \frac{|\dot{\phi}|}{|\dot{\beta}|} \, \alpha \, - \frac{|C \gamma|}{|\dot{\beta}|} = \, 0$$

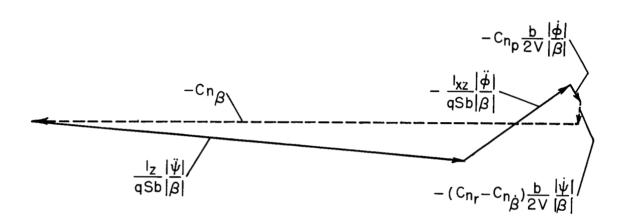
Figure 12.- Typical vector solution; body-axis system.



Rolling-moment equation:

$$\frac{|\textbf{x}|}{|\textbf{qSb}|}\frac{|\ddot{\phi}|}{|\beta|} - \frac{|\textbf{xz}|}{|\beta|}\frac{|\ddot{\psi}|}{|\beta|} - C_{l_r}\frac{b}{2V}\frac{|\dot{\psi}|}{|\beta|} - C_{l_p}\frac{b}{2V}\frac{|\dot{\phi}|}{|\beta|} - C_{l_\beta} = 0$$

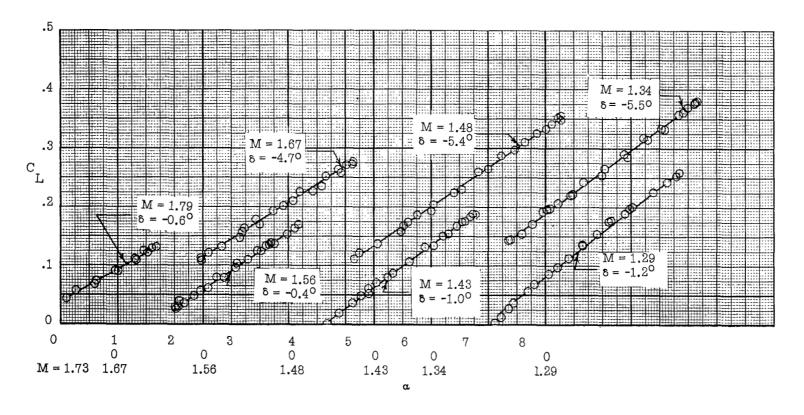
Figure 12.- Continued.



Yawing-moment equation

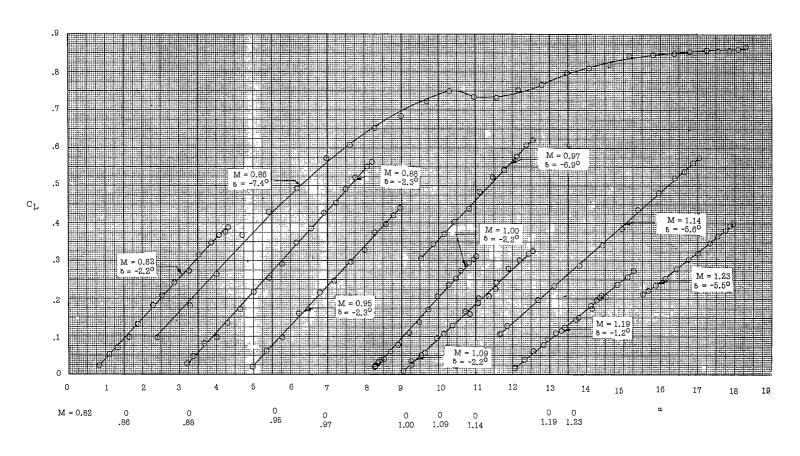
$$\frac{|z|}{|\beta|} \frac{|\ddot{\psi}|}{|\beta|} - \frac{|xz|}{|\beta|} \frac{|\ddot{\phi}|}{|\beta|} - C_{np} \frac{b}{2V} \frac{|\dot{\phi}|}{|\beta|} - (C_{nr} - C_{n\dot{\beta}}) \frac{b}{2V} \frac{|\dot{\psi}|}{|\beta|} - C_{n\beta} = 0$$

Figure 12.- Concluded.



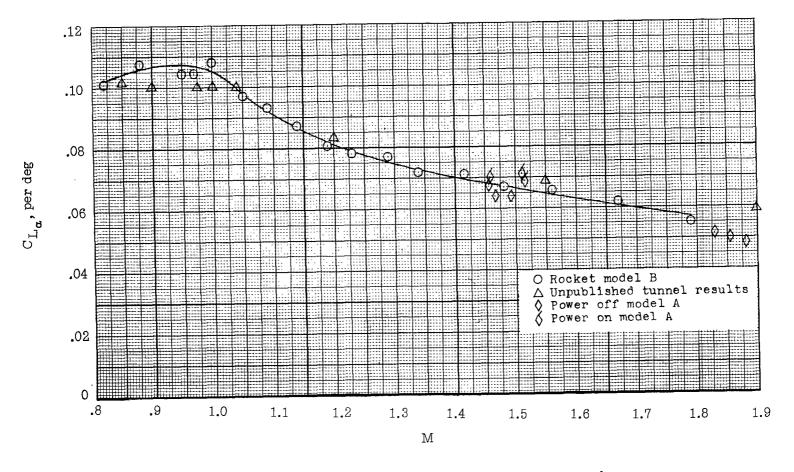
(a) Lift coefficient as a function of angle of attack.

Figure 13.- Lift characteristics of model B.



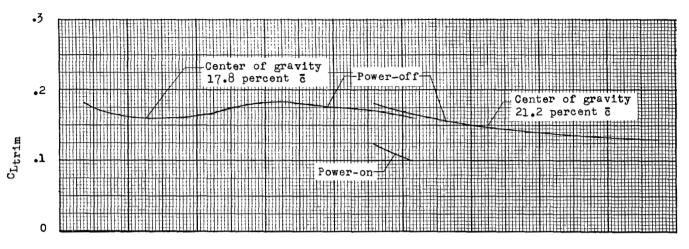
(a) Concluded.

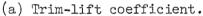
Figure 13.- Continued.

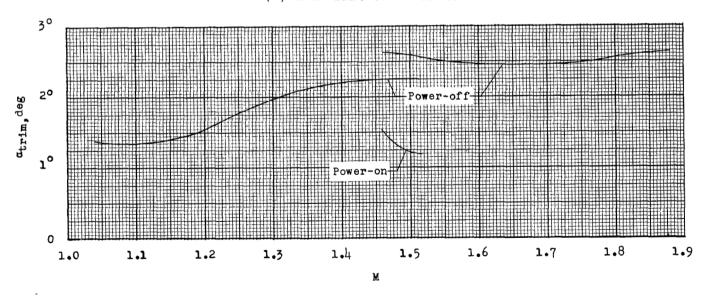


(b) Variation of lift-curve slope with Mach number.

Figure 13.- Concluded.

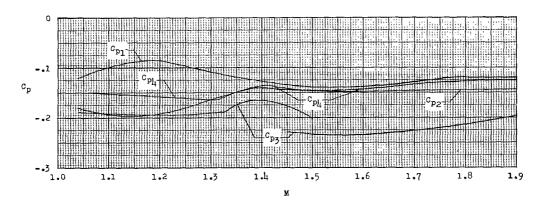




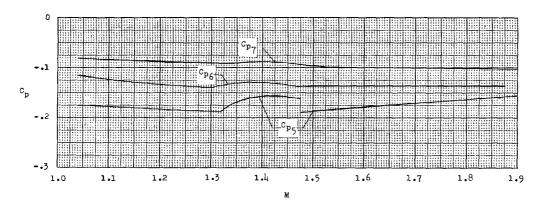


(b) Trim angle of attack.

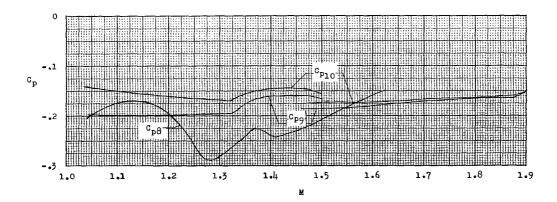
Figure 14.- Power-on and power-off variation of trim conditions with Mach number.



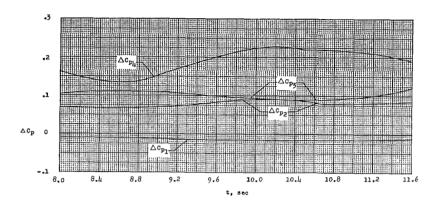
(a) Orifices 1, 2, 3, and 4 (bottom of fuselage).



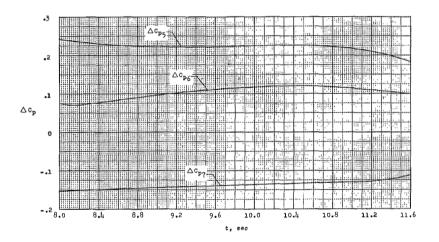
(b) Orifices 5, 6, and 7 (side of fuselage).



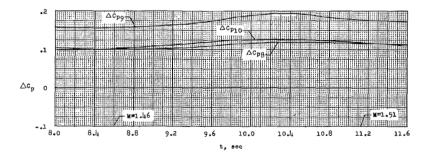
(c) Orifices 8, 9, and 10 (horizontal stabilizer and nacelle base). Figure 15.- Power-off pressure-coefficient variation with Mach number.



(a) Orifices 1, 2, 3, and 4 (bottom of fuselage).



(b) Orifices 5, 6, and 7 (side of fuselage).



(c) Orifices 8, 9, and 10 (horizontal stabilizer and base).

Figure 16.- Variation with time of the incremental change in pressure coefficient due to power effects.

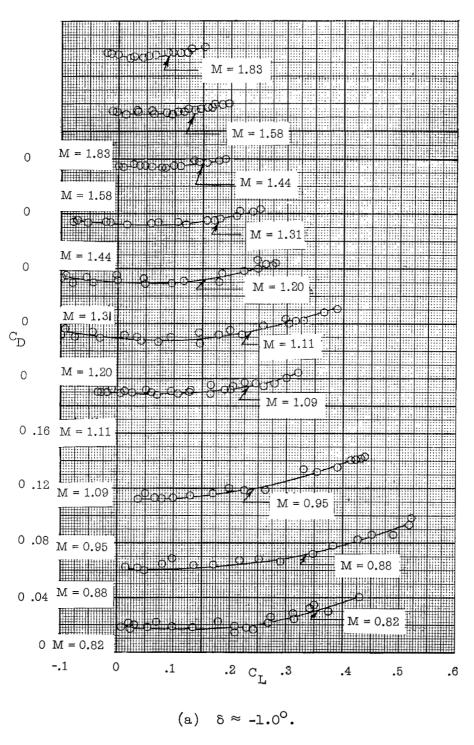
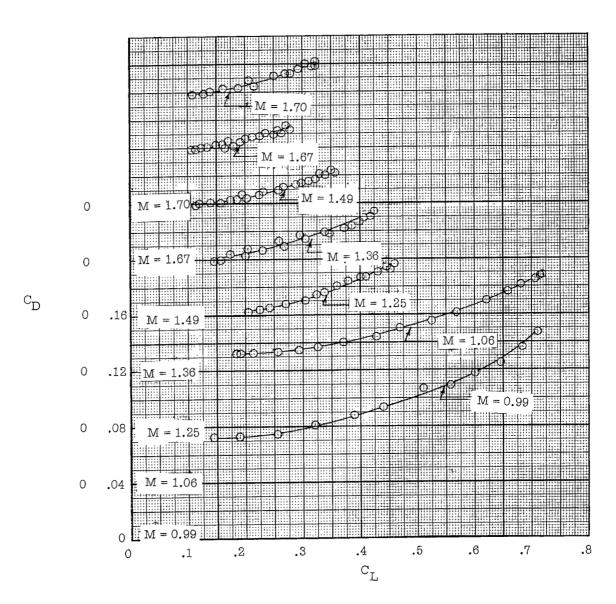


Figure 17.- Variation of drag coefficient with lift coefficient from model B. Drag coefficient includes internal and base drag.



(b) $\delta \approx -5.5^{\circ}$.

Figure 17.- Concluded.

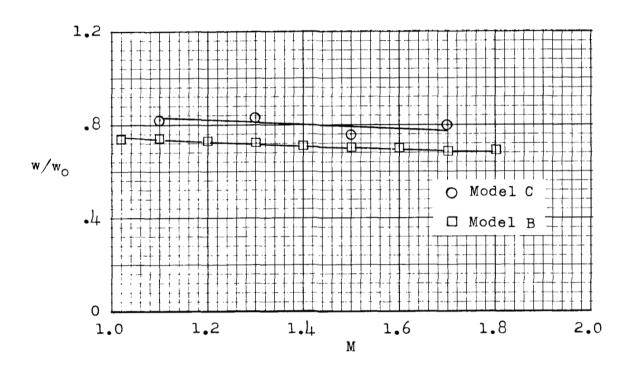


Figure 18.- Duct mass-flow ratio.

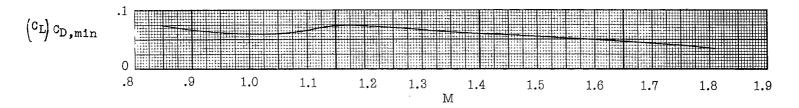


Figure 19.- Lift coefficient for minimum drag.

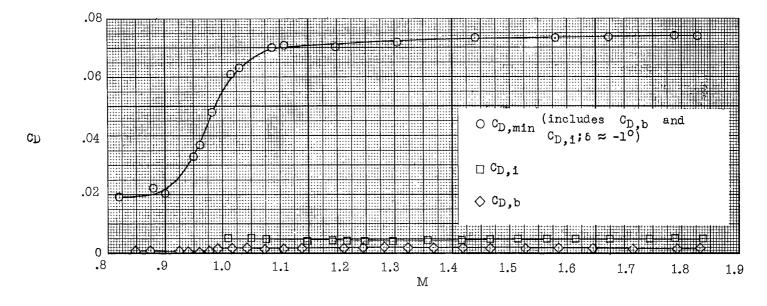


Figure 20.- Drag coefficient as a function of Mach number (from model B).

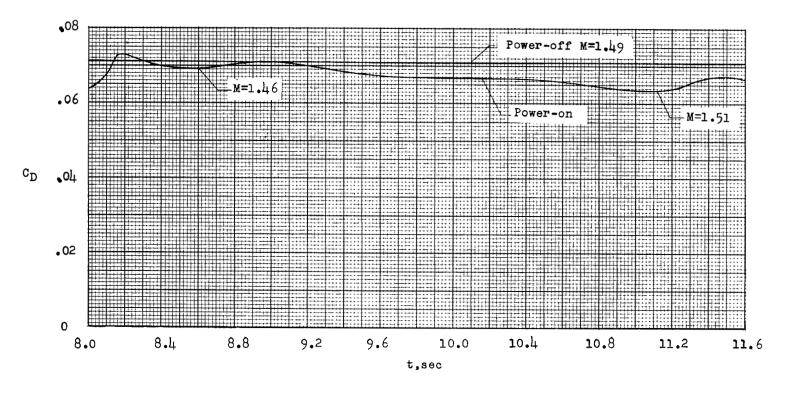
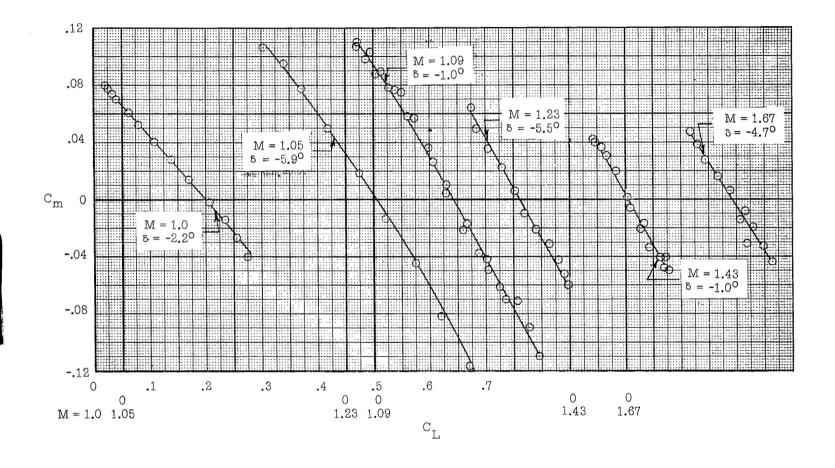
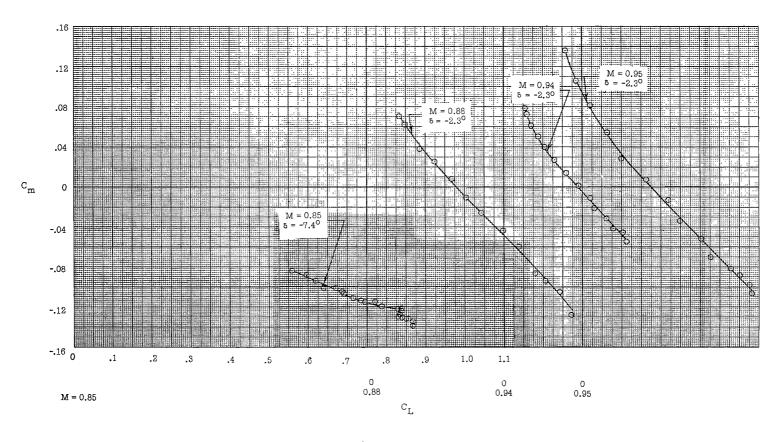


Figure 21.- The variation of power-on drag coefficient with time for a lift coefficient of 0.011. Power-off external drag coefficient for $C_{\rm L}$ = 0.11 shown for comparison.



(a) $M \ge 1.0$.

Figure 22.- Variation of pitching-moment coefficient with lift coefficient. Center of gravity at 0.169c; model B.



(b) M < 1.0.

Figure 22.- Concluded.

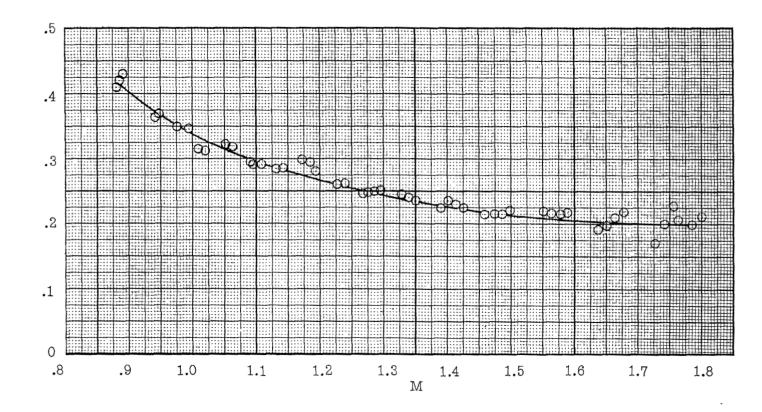


Figure 23.- Period of the longitudinal oscillation. Model B.

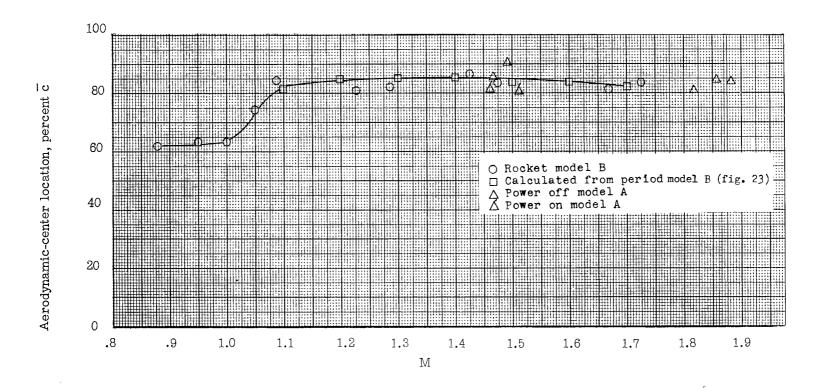


Figure 24.- Aerodynamic-center location.

- Rocket-model test

Figure 25.- Basic pitching-moment coefficient.

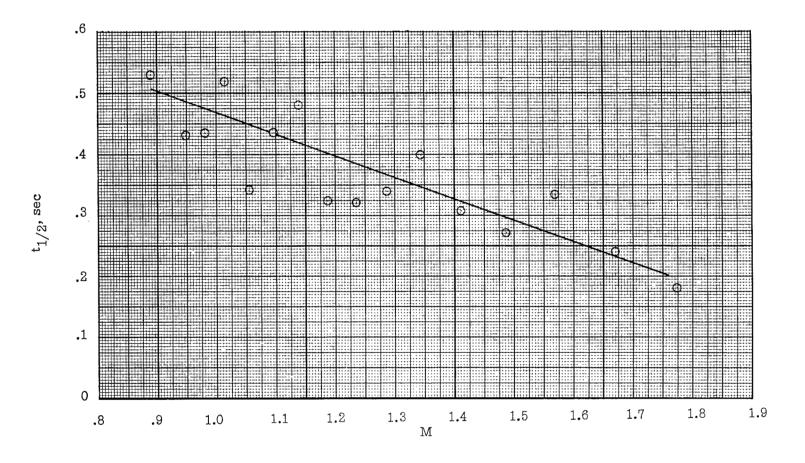


Figure 26.- Time to damp to half amplitude. Model B.

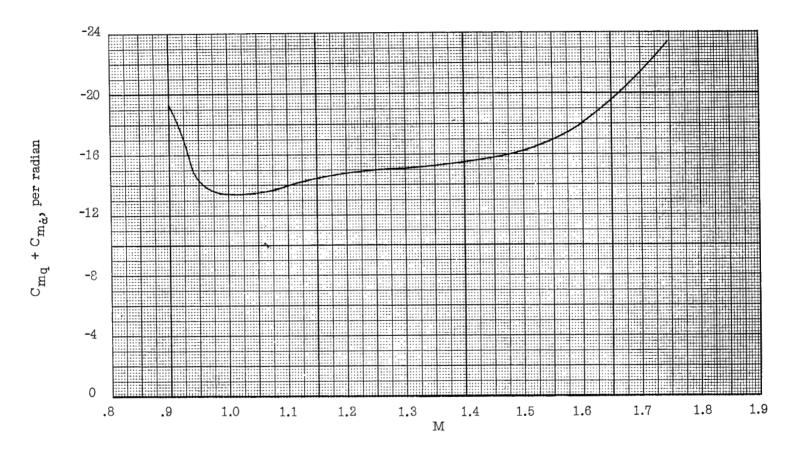


Figure 27.- Pitch-damping parameter. Center of gravity at 0.169c; model B.

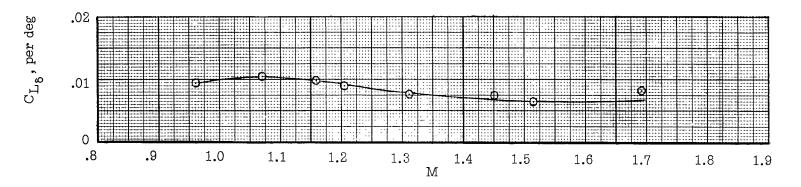


Figure 28.- Control lift effectiveness. Model B.

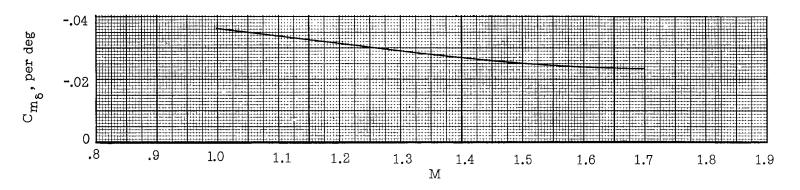


Figure 29.- Control pitching effectiveness. Center of gravity at 0.1695; model B.

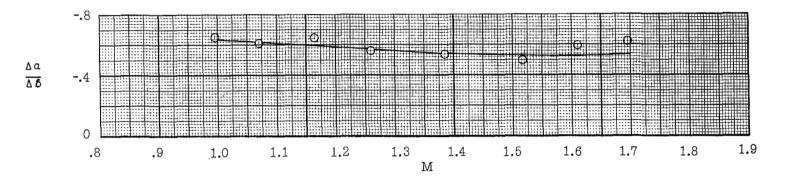


Figure 30.- Change in angle of attack per degree of tail deflection.

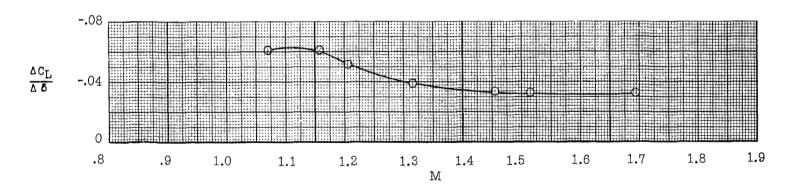


Figure 31.- Change in lift coefficient per degree of tail deflection.

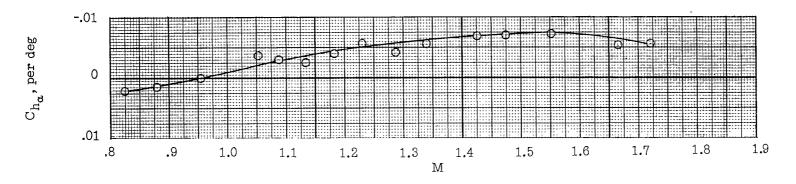


Figure 32.- Effect of Mach number on $C_{\mathbf{h}_{\alpha}}$. Model B.

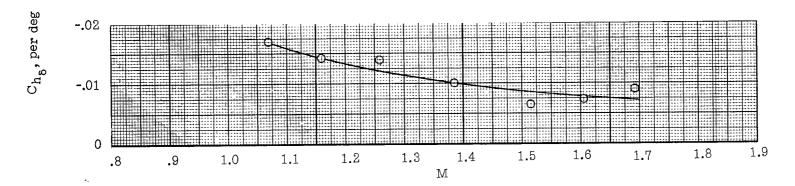
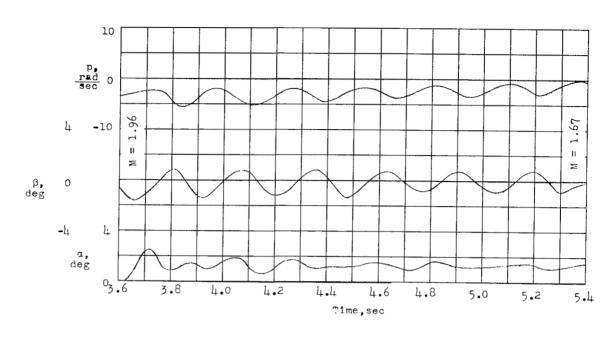


Figure 33.- Effect of Mach number on $\text{C}_{h_{\mbox{$\delta$}}}.$ Model B.



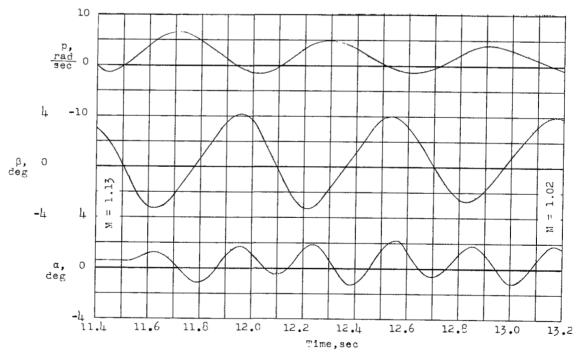


Figure 34.- Time history of some of the quantities measured. Model C.

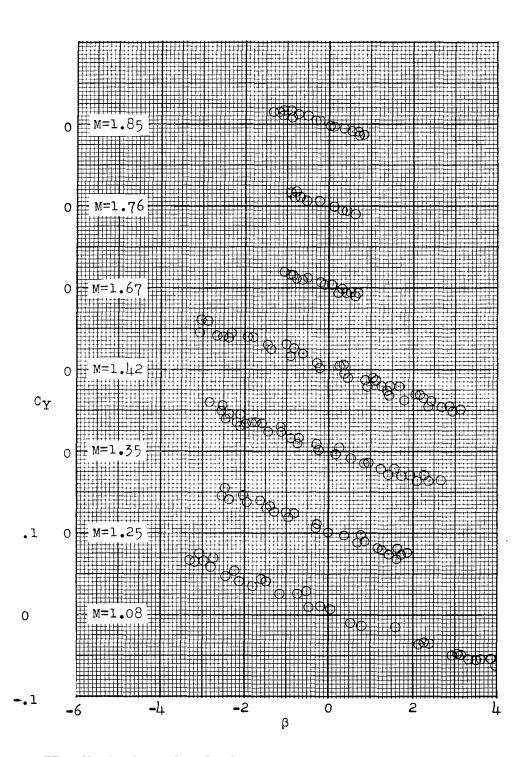


Figure 35.- Variation of side-force coefficient with angle of sideslip. Model ${\tt C.}$

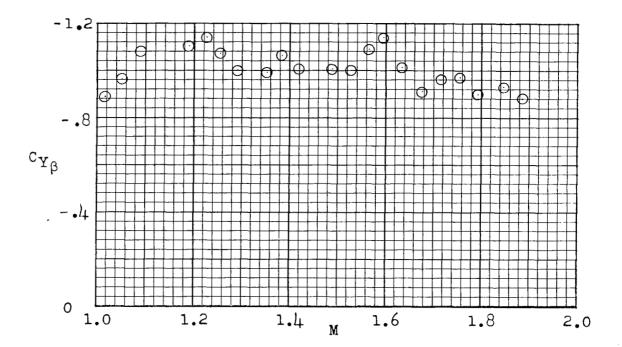


Figure 36.- Side force due to angle-of-sideslip derivative. Model C.

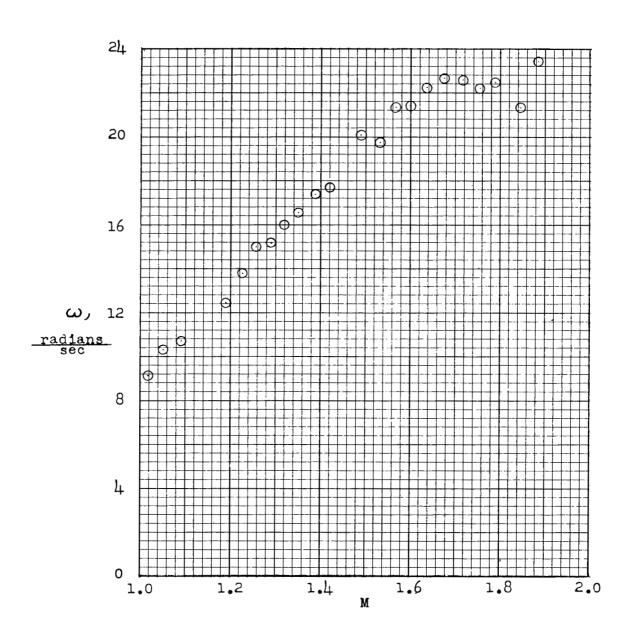


Figure 37.- Frequency of Dutch roll oscillations. Model C.

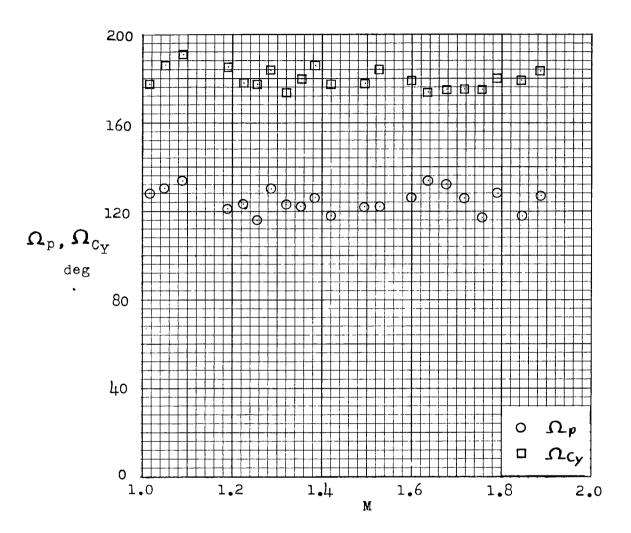


Figure 38.- Phase angles of roll rate and side-force coefficient to angle of sideslip. Model C.

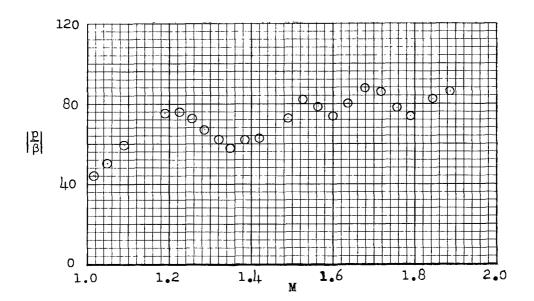


Figure 39.- Amplitude ratio of roll rate to angle of sideslip. Model C.

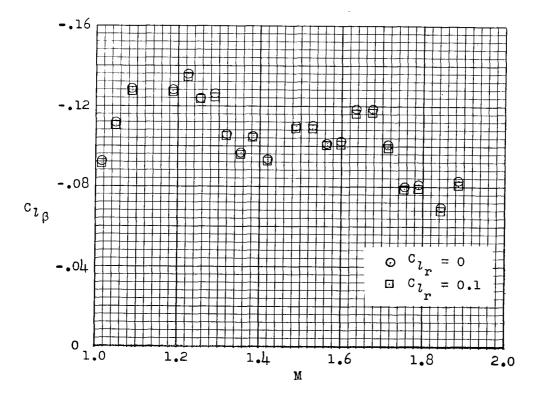


Figure 40.- Dihedral-effect derivative. Model C.

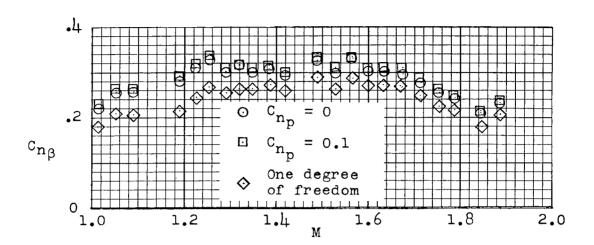


Figure 41.- Static lateral stability. Model C.

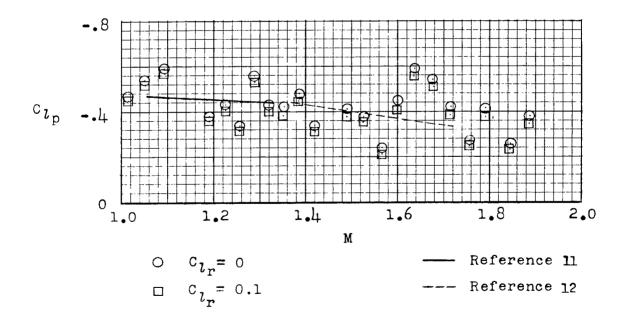


Figure 42.- Roll-damping derivative. Model C.

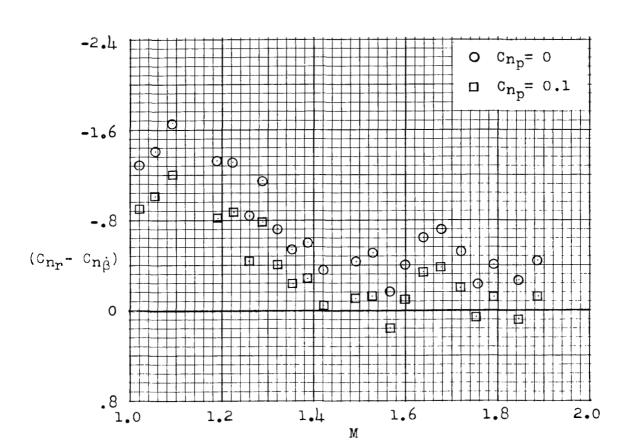
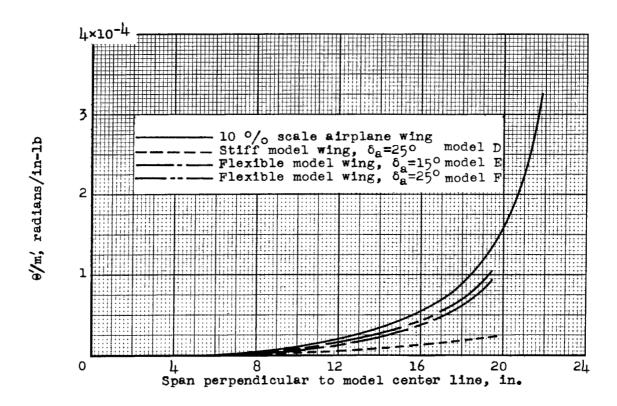


Figure 43.- Dynamic-lateral-stability derivative. Model C.



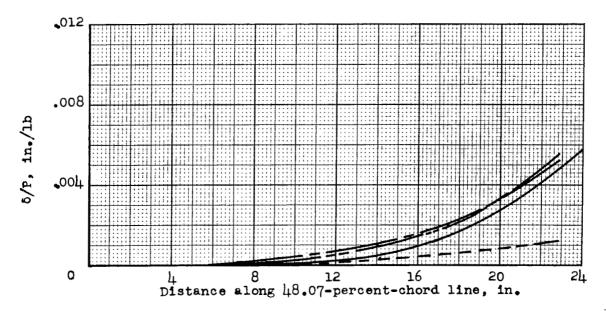


Figure 44.- Stiffness characteristics of model wings compared with scaled stiffness airplane wing.

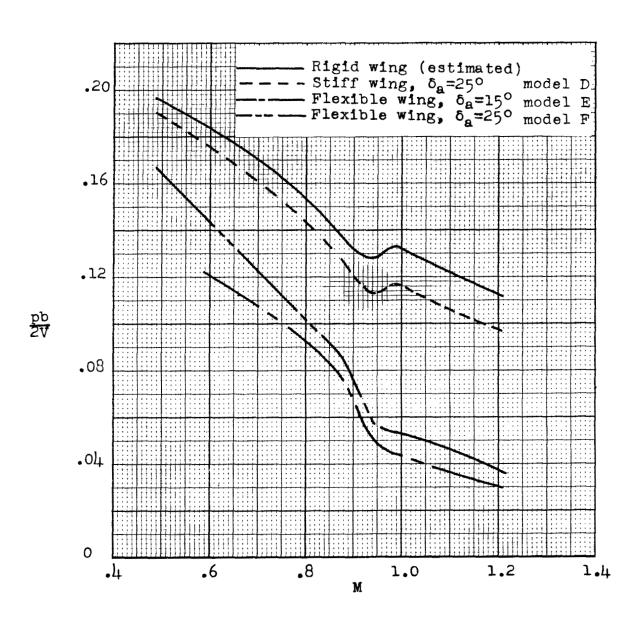


Figure 45.- Variation of rolling effectiveness parameter pb/2V with Mach number.

ŀ

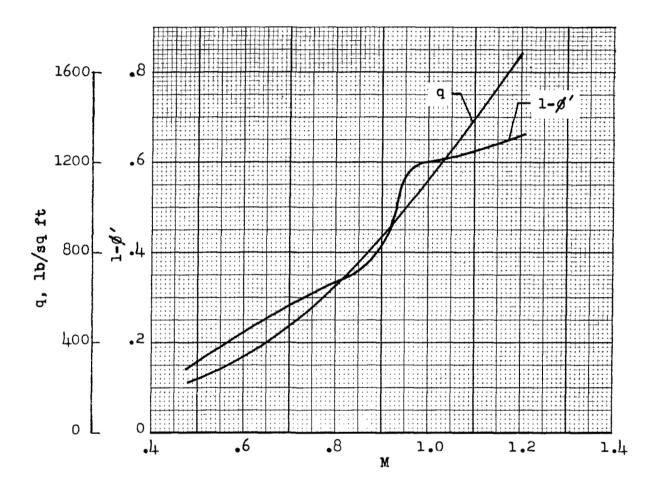


Figure 46.- Variation with Mach number of q and l- ϕ' for the flexiblewing model with 25° aileron deflection.

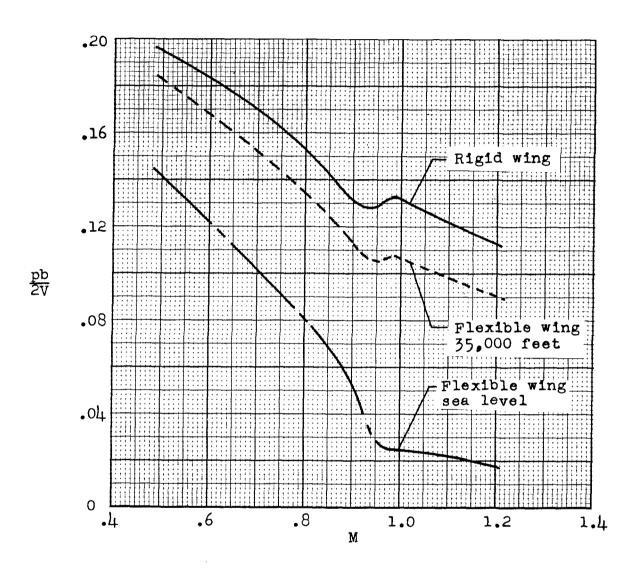


Figure 47.- Comparison of rolling effectiveness of the flexible wing at sea level and 35,000 feet with rigid-wing rolling effectiveness. δ_a = 25°.



